UNIVERSITY OF OKLAHOMA

GRADUATE COLLEGE

DAMAGE ZONE CHARACTERIZATION USING COHERENCE & REJECTED NOISE DERIVED FROM STRUCTURE ORIENTED FILTERING

A THESIS

SUBMITTED TO THE GRADUATE FACULTY

in partial fulfillment of the requirement for the

Degree of

MASTER OF SCIENCE

By

JARED WILLIAM BROWN

Norman, Oklahoma

2026

DAMAGE ZONE CHARACTERIZATION USING COHERENCE & REJECTED NOISE DERIVED FROM STRUCTURE ORIENTED FILTERING

A THESIS APPROVED FOR THE

SCHOOL OF GEOSCIENCES

BY THE COMMITTEE CONSISTING OF

Dr. Heather Bedle, Chair

Dr. Brett M. Carpenter

Dr. Matthew Pranter

ACKNOWLEDGEMENTS

If I am lucky enough to have a career I can look back on proudly, there will undoubtedly be several key mentors who helped put me in that position. I know that one of the first people I'll be thinking of is Dr. Heather Bedle. It was not until she welcomed me into the AASPI consortium that I started to get opportunities to showcase my abilities in a professional capacity, and I will forever be indebted to her due to that fact. Thank you for all the kindness you've showed me during my time at the University of Oklahoma, I will not forget it.

With that said, I would also like to thank Dr. David Lubo-Robles, Dr. Kurt Marfurt, and the rest of the AASPI researchers for their support, letting me learn from them, and the memories made. I would also like extend my thanks to my other committee members, Dr. Brett Carpenter and Dr. Matthew Pranter, who were always open to listen to any question of mine and have given me invaluable guidance. Everyone I've mentioned helped contribute to a very collaborative learning environment and are the reason that I won't relate to other people if I hear them complain about how terrible of an experience graduate school was.

For the data used in this study, I would like to thank Marcilio Matos, Marcus Maas, and Petrobras, the National Archives for Marine Seismic Surveys, and New Zealand Petroleum & minerals.

Lastly, I would like my family, particularly my Mom and Dad. They have been unbelievably supportive of me my entire life. Seeing them excel in their respective careers growing up gave me an incredibly strong mentality when approaching academics. Giving up never felt like an option or a thought that crossed my mind, which was especially helpful in the later years of my undergraduate coursework where the teaching content got difficult for me. I am so grateful for all that you guys have done for me.

CONTENTS

LIST OF FIGURES

ABSTRACT

As seismic attributes were first incorporated into academic and industry workflows, fault detection and visualization became a primary objective. Faults and their associated damage zones exert significant control on subsurface fluid flow, seal integrity, and reservoir compartmentalization. While attributes such as coherence have proven effective for delineating fault geometries, quantitative workflows for constraining fault damage zone widths from seismic data remain underdeveloped.

This study investigates the use of coherence and rejected noise derived from structure-oriented filtering (SOF) to characterize fault damage zones within the Bacalhau 3D seismic dataset in the post-salt interval of the Santos Basin. Coherence consistently delineated fault geometries and produced damage zone width estimates comparable to field-based outcrop measurements, reproducing the near 1:1 linear scaling relationship between fault slip and damage zone width documented in field studies. Rejected noise frequently mimicked seismic stratigraphy, reducing its reliability for estimating fault zone widths. However, noise aligned with interpreted faults was morphologically distinct and enhanced continuity along small-offset faults that do not register a coherence anomaly. At times, rejected noise also modeled a substantially wider damage zone than coherence.

In the pre-salt carbonates of the Bacalhau field, well data indicated that coherence primarily responds to the most intensely fractured intervals, whereas rejected noise is more sensitive to mechanical and petrophysical transitions, capturing shifts from tight rock to porous and/or fractured rock not resolved by coherence. These results demonstrate that coherence and SOF-derived noise are complementary attributes, and when integrated with well data, can provide a more robust framework for seismic characterization of fault damage zones.

Damage Zone Estimation Using Coherence & Rejected Noise Derived from Structure-Oriented Filtering

INTRODUCTION

Background & Motivation

Two decades after the emergence of seismic attributes in the early 1970s, the introduction of coherence attributes marked a significant advancement in seismic interpretation. Their ability to clearly delineate geologic features such as faults, channels, and karst systems fundamentally reshaped the analysis of 3D seismic data (Chopra & Marfurt, 2005). Subsequently, a processing technique emerged which is commonly used in tandem with coherence: structure-oriented filtering (SOF). SOF uses coherence as an input that selectively filters the most coherent seismic trace, thereby suppressing cross-cutting and random noise while preserving low-coherence features more likely related to geologic structures such as faults and unconformities (Chopra & Marfurt, 2017; Fehmers & Hocker, 2003). Observations of anomalous rejected noise concentrated along faults suggest that when evaluated alongside coherence, it may provide complementary information relevant to fault zone architecture and improve constraints on estimating damage zone width in 3D seismic data.

We defined damage zones as regions of secondary fracturing, pulverization, and deformation that propagate outward from the fault plane as displacement increases. Figure 1 illustrates an example of damage zone architecture, though damage zones are not always bounded by subsidiary faults as shown. Damage zone extent may also be expressed as increased deformation above an interpreted background level. Workflows for quantifying damage zone extent at the seismic scale remain limited, as conventional interpretations typically just determine the presence of a fault, rather than providing information on the surrounding damage zone. When using 3D seismic data, we don't know for certain what type of structures represent the damage zone (e.g. fractures, subsidiary faults, deformation bands, and/or pulverized rock) but our results indicate that at best, the rejected noise could potentially be sensitive to zones with an increased occurrence of damage structures on the order of meters in length For our purposes, structures of this magnitude would define the outermost extent of the damage zone in this seismic survey, the details of which are later described below.

Accurate characterization of damage zone extent is critical because these regions strongly influence subsurface deformation and fluid migration. Improved estimates of damage zone width can help mitigate drilling hazards by better anticipating fractured intervals, enhance assessment of seal rock integrity, and refine predictions of reservoir compartmentalization and connectivity. These considerations extend beyond hydrocarbon exploration, as accurately quantifying constraints on damage zones are equally critical for subsurface storage of CO_2, geothermal energy projects, and hydrogen exploration/storage. Improving seismic-based estimates of damage zone thickness is likely to enhance confidence in evaluating both hydrocarbon reservoirs and these emerging sustainable energy endeavors.

Coherence has been used to approximate damage zone thickness (Liao et al. 2019), however, relationships between these seismic-based estimates and outcrop studies remain insufficiently explored. This disconnect is partly attributable to differences in scale and resolution, as seismic data often resolves features on the order of tens to hundreds of meters, whereas outcrop observations capture much finer structural detail. Some studies have even used microfracture/microstructure density to distinguish between the damage zone and protolith (Faulkner et al., 2011; Shipton & Cowie, 2001). More broadly, it is observed in literature that damage zone width increases with fault displacement. To bridge this gap between seismic and field data, the selected 3D survey should be high resolution, depth converted and include faults exhibiting a range of slip magnitudes. This is why the Bacalhau 3D survey was selected for this study. It contains a heavily faulted section that extends through Upper Cretaceous rock units, with fault slip ranging from approximately 20 to 100 meters at an estimated vertical resolution of 10 meters. Well data is also available to supplement these observations. Although the wells primarily targeted the lower Cretaceous Barra Velha Formation approximately 2 km deeper, the tested intervals occur in rocks strongly influenced by proximal syn-rift faults, which acted as hydrothermal conduits promoting diagenetic alteration within the formation (Maas et al. 2025).

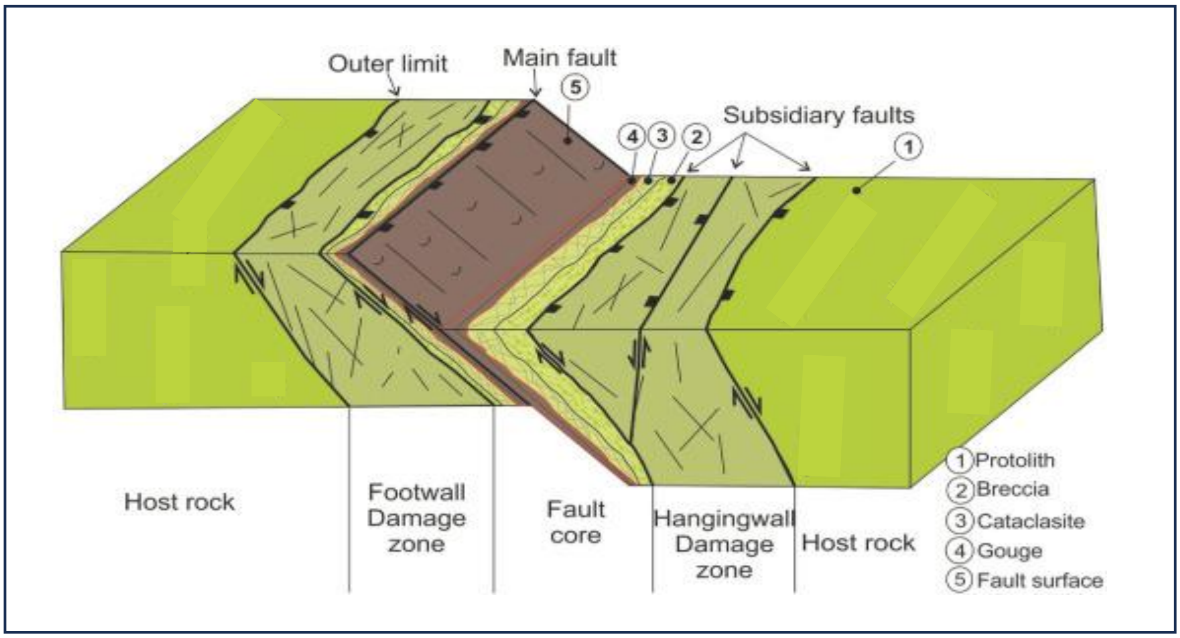

Figure 1. Schematic illustration of fault zone architecture showing the fault core and surrounding hanging wall and footwall damage zones. The damage zone consists of fractured and deformed host rock adjacent to the fault core, which may contain breccia, cataclasite and gouge. Accumulated slip on the primary fault redistributes stress into the surrounding rock, causing localized failure on newly oriented planes that can develop as subsidiary faults. Modified from Celestino et al. (2020).

Coherence

The coherence attribute used in this study is energy-ratio similarity, defined as the ratio of coherent energy to total energy within the analysis window. Details of how these energy terms are calculated are provided by Chopra and Marfurt (2018). When seismic traces within the analysis window mirror one another and exhibit strong lateral continuity, coherent energy is roughly equal to total energy, making the ratio approximately 1. As seismic trace variability increases, a smaller fraction of the total energy is considered coherent, causing the ratio to decrease. As energy-ratio similarity decreases from 1, waveform dissimilarity increases and may reflect structural discontinuities such as faults, unconformities, or channel edges. It is important to note however that regions in seismic amplitude data with poor signal-to-noise ratio can also produce low similarity values.

SOF

Structure-oriented filtering (SOF) is a processing method that removes noise while preserving structures that exhibit lower coherence such as faults and unconformities. This rejected noise served as a tool to directly estimate damage zone widths in conjunction with coherence. We used Marfurt's (2006) technique that combines Kuwahara et al.'s (1976) use of over-lapping analysis windows and Luo et al.'s (2002) edge preservation smoothing algorithm. The approach uses 3D overlapping analysis windows, that analyze the coherence of the seismic traces that reside within it. The trace with the highest coherence is selected for filtering, thus preserving the traces that are more likely related to structural discontinuities (Figure 2). The filtering itself involves several steps. First, the seismic data is sampled parallel to structural dip, and vertically interpolated trace by trace to form vectors representative of each seismic trace or "sample vectors" within the 3D analysis window. The vectors are then compiled to form a covariance matrix where the eigen vectors (or "eigen maps") are computed. These vectors show the data's direction of greatest variability which tend to be related to seismic signal rather than noise. The seismic trace is then reconstructed by projecting the local sample vector onto the leading eigenvectors by computing the dot product between them, and then summing these scaled eigenvectors, also known as principal components, to form the filtered trace. The difference between the original seismic trace and the new filtered trace is the rejected noise. The amplitudes and spatial behavior of this noise was used in concert with coherence to interpret damage zone extent.

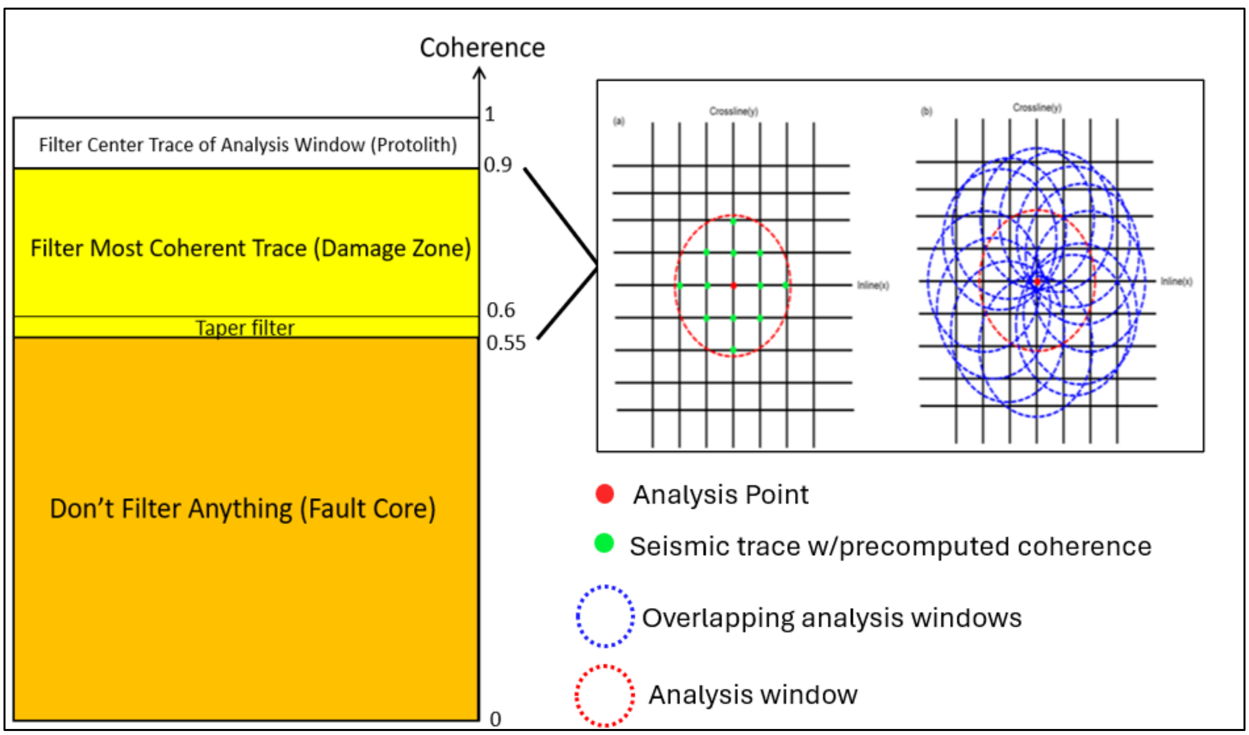

Figure 2. SOF framework. Left side of image shows what SOF does depending on the coherence values of the traces that fall within the analysis window. The 0.9, 0.6, and 0.55 are user defined coherence thresholds. The image on the right side depicts a Kuwahara filter on a seismic inline & crossline grid which "searches" for the most coherent trace within the window to filter so that the less coherent traces that are more likely related to geologic structures are preserved.

Novel Contributions

Although the term "rejected noise" suggests an unwanted processing artifact, we use it here to describe the residual signal removed by SOF, which may contain geologically meaningful information that could be used as an interpretive seismic attribute. In this study's context, rejected noise preserves the portion of the seismic signal not represented by the dominant amplitude pattern, which potentially contains information related to smaller-scale structural complexities within fault damage zones. Considered together, these attributes may provide complementary perspectives on fault zone structure, with coherence emphasizing broader fault zone features and rejected noise highlighting localized structural complexity. In this study, we treated SOF-derived rejected noise as a seismic attribute for direct structural interpretation rather than solely a processing byproduct that is only checked for QA/QC of seismic amplitude data. We tested whether noise, when evaluated alongside coherence can provide reasonable damage zone estimates, with field studies and available well control being used as our validation.

With the objectives and contribution of this study established, we next describe the seismic datasets to which the workflow is applied. The following section summarizes the Bacalhau 3D seismic survey and additional comparative seismic volumes.

SEISMIC DATA

The primary analysis of this study focuses on the Bacalhau 3D seismic dataset, located in the Santos Basin offshore Brazil, which was acquired in 2002 and processed in 2014 through Kirchhoff pre-stack depth migration. The Bacalhau volume has a bin size of 25 by 25 m, a vertical sample interval of 5 m, azimuthal coverage of approximately 270 degrees, and a maximum offset of 6,200 m. To evaluate how noise appears in other seismic datasets, we conducted comparative interpretations using two additional 3D time-migrated datasets: the Matagorda Island merge from the Texas Shelf, combining legacy surveys acquired in 1991 and 1994, and the Great South Basin dataset acquired in 2007, offshore New Zealand.

Having described the seismic dataset used in this study, it is important to place the analysis within its regional geologic framework. The structural and stratigraphic architecture observed in the seismic data is fundamentally tied to the tectonic and depositional history of the basin. The Bacalhau field in the Santos Basin provides a particularly suitable setting for this analysis, as extensive faulting associated with rifting and later salt tectonics has created a structurally complex system where faults are well developed and observable in this seismic dataset. The following section summarizes the geologic evolution relevant to the study area.

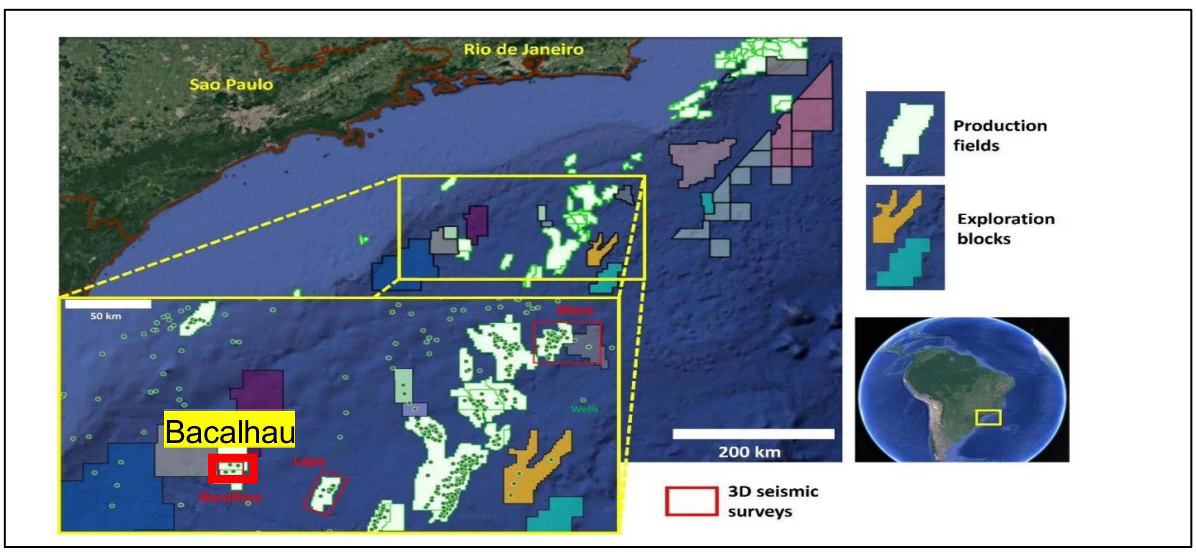

Figure 3. Area of interest. The Bacalhau survey is highlighted in bold red, the 2 other outlined surveys that are not included in this study are the Mero, and Lapa surveys. Image is modified from Maas et al. (2025).

GEOLOGICAL SETTING

A representative cross section of different fields, including Bacalhau is shown in Figure 4. Located off the shore of SE Brazil, this basin began subsiding in the early Cretaceous as Gondwana began to split, opening up the South Atlantic. Early rifting in the Hauterivian was accompanied by major volcanism along fault zones, depositing thick flood basalts of the Camboriu Formation on top of the Paleozoic basement (Baptista et al., 2023).

Over these basalts, continued syn-rift subsidence created a compartmentalized lacustrine setting, where deeper areas accumulated Mg-rich clays while proximal margins received conglomerates and fluvio-deltaic sandstones that make up the basal syn-rift Picarras Formation. The organic rich lacustrine shales of the Picarras Formation constitute the primary source rock of the pre-salt petroleum system. As rifting continued into the lower Aptian, more shales were deposited in the deep lacustrine settings, while shallow to marginal settings accumulated heterogeneous high-energy carbonates, including coquina deposits that constitute the Itapema Formation (Baptista et al., 2023). In the Bacalhau field, complex paleo topography developed during periods of enhanced volcanism which led to limited accommodation space for deposition of the Itapema Formation along structural highs within the survey area (Louback et al., 2023).

After a subsequent erosional period with concurrent lithospheric cooling, further subsidence promoted renewed carbonate accumulation leading to the formation of the Barra Velha Formation, the main reservoir of the pre-salt play. This system is characterized by carbonate build-ups, platforms, and mound facies. Certain areas developed from hydrothermal alteration where hot, silica rich fluids used deep seated syn rift faults as migration pathways to percolate into the formation, creating high grade reservoir properties (Maas et al., 2025).

In the late Aptian, a failed rift system caused a relief low, which flooded the lake environment with pulses of sea water. Over time, this led to the accumulation of thick evaporites, reaching 2 km thick in certain areas, constituting the Ariri Formation (Moreira et al., 2007). The Ariri Formation is what separates the Santos Basin from its pre and post-salt depositional sequences/petroleum systems (Figure 5).

During the Albian, as sea levels rose, marine conditions became more established, beginning with shallow-water deposits which included shales, marls, carbonates, and high-energy oolitic/bioclastic limestones (Guaruja Formation), with fluvial/deltaic sandstones in more proximal settings (Itanhaem Formation). A marine drift/transgressive mega-sequence then persisted into the late Cretaceous, depositing interlayered sandstones and siltstones (Jureia, and Itajai-Acu Formations), with reservoir quality turbidites (Baptista et al., 2023). The faults zones quantified in this study post-date the Ariri Formation and likely developed due to salt evacuation during the upper Cretaceous.

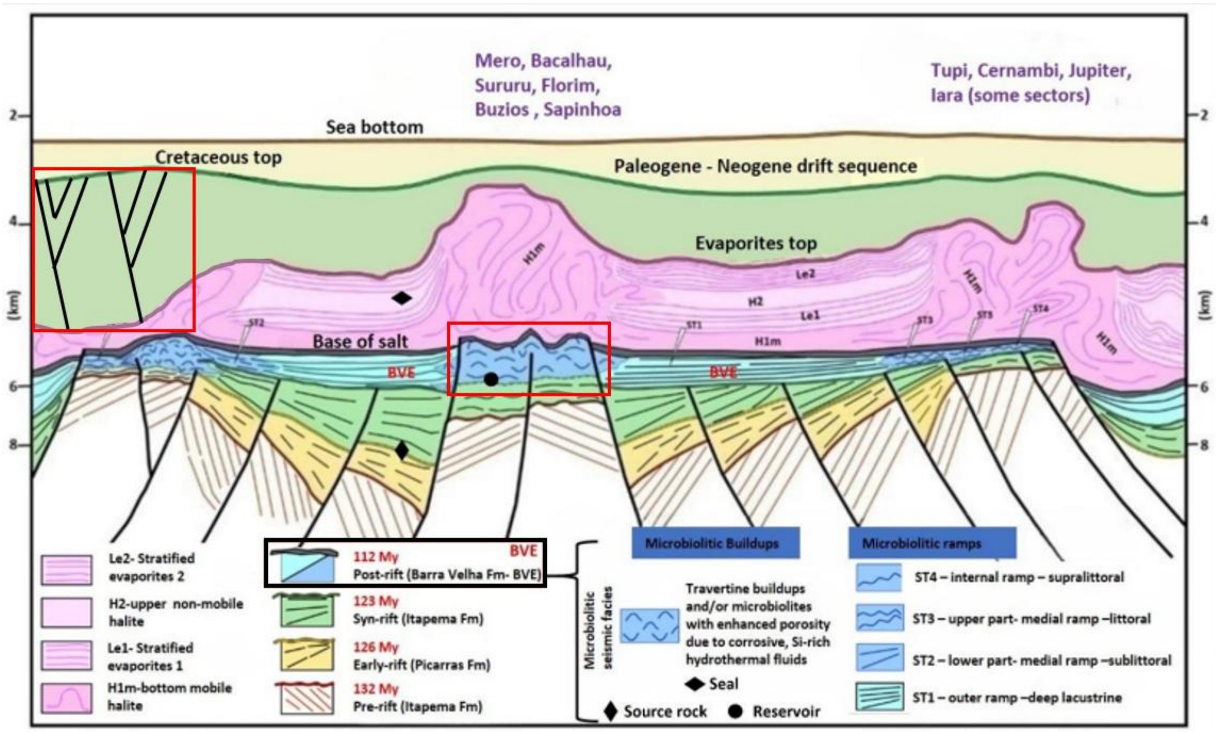

Figure 4. Geologic cross section. Depicts the general geologic trends between different oil fields in the Santos Basin. The faulted upper Cretaceous system on the left-hand side outlined in red was altered to represent the northern-most section of the Bacalhau seismic survey where we measure damage zone widths from extensional faults that likely developed along with the evacuation of the underlying Ariri Formation. The Barra Velha reservoir outlined in red represents where we have well control in our seismic survey. Modified from Maas et al. (2025).

The following section describes the workflow used in this study, including the interpretation of the damage zone-protolith boundary from seismic data, the methodology for fault zone width estimation, and how we utilized outcrop measurements, well data, and core reports as a means of external support for our analyses.

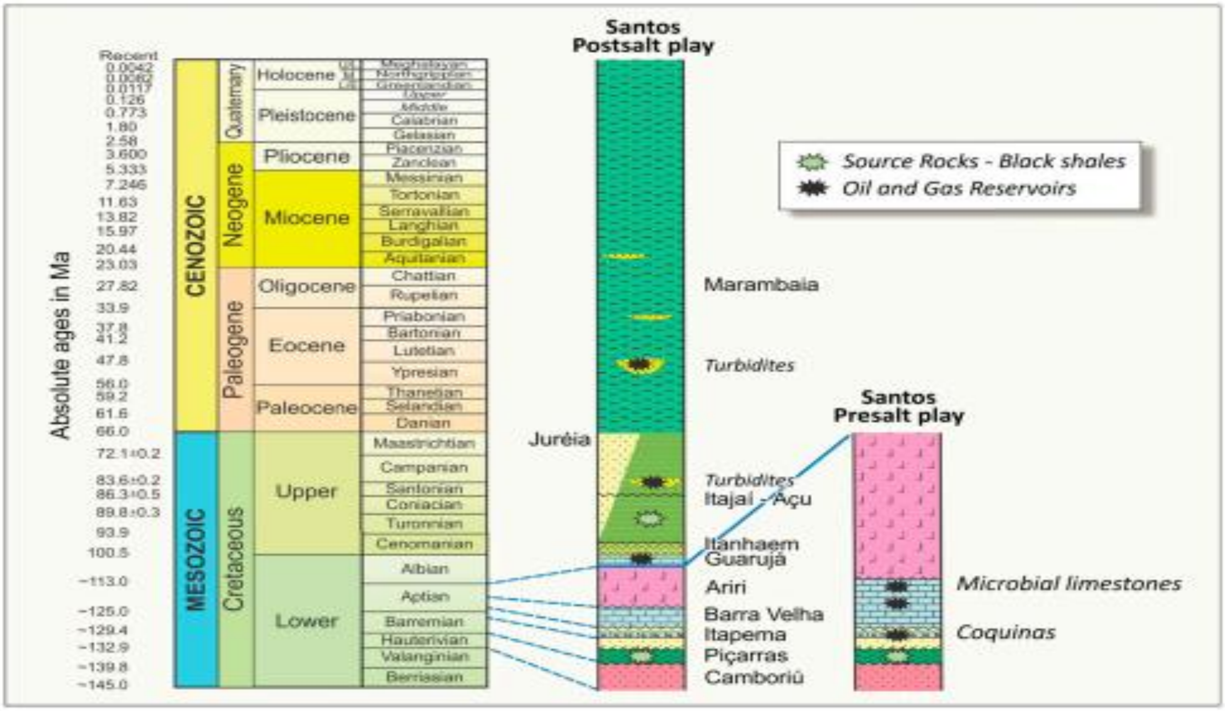

Figure 5. Stratigraphic column for Santos Basin. The petroleum systems of both the pre and post-salt systems are described on the right side of the figure with the source and reservoir rocks labeled accordingly. Reproduced from Baptista et al. (2023)

METHODOLOGY

Attribute Computation

After selecting a faulted area of interest, we calculated energy ratio similarity on our seismic volume using a pre-computed dip volume as input. Subsequently, we applied structure-oriented filtering (SOF) to the data. Figure 6 illustrates the workflow used in this study.

Traditionally, the interpreter applies a cut-off parameter such that traces below a specified coherence value interpreted to be fault-related are preserved and excluded from filtering to avoid smoothing structural discontinuities. However, because this study focused on noise generated by structural features, we nullified this parameter by setting it to zero.

Coherence-Based Damage Zone Boundaries

To determine the non-zero coherence threshold defining the boundary between protolith and damage zone (parameter shown in Figure 2) we established what coherence values corresponded to the outer edges of damage zones within the seismic dataset. To accomplish this, we applied a rainbow color bar with a continuous gradient to a time slice at the depth of the characterized faults. Coherence values that exhibited structurally continuous regions devoid of deformation (protolith) were mainly between 0.95 and 1. The highest coherence values that were able to delineate fault planes were found to be approximately 0.85–0.86 (Figure 7). This indicates that the range of coherence values marking the transition between protolith and damage zone is roughly 0.94–0.87. Therefore, 0.9 was determined to be a reasonable threshold, as it lies comfortably between these upper and lower bounds, and is consistent with the threshold reported by Liao et al. (2019) for damage zone extent in a seismic survey of the El Reno Fault Zone in the Anadarko Basin.

This threshold selection is interpreter-guided and therefore introduces some uncertainty, however, the magnitude of this uncertainty is limited. Across the sampling lines, selecting 0.94 versus 0.87 as the separation threshold changes estimated damage zone width by 10–15 meters on average.

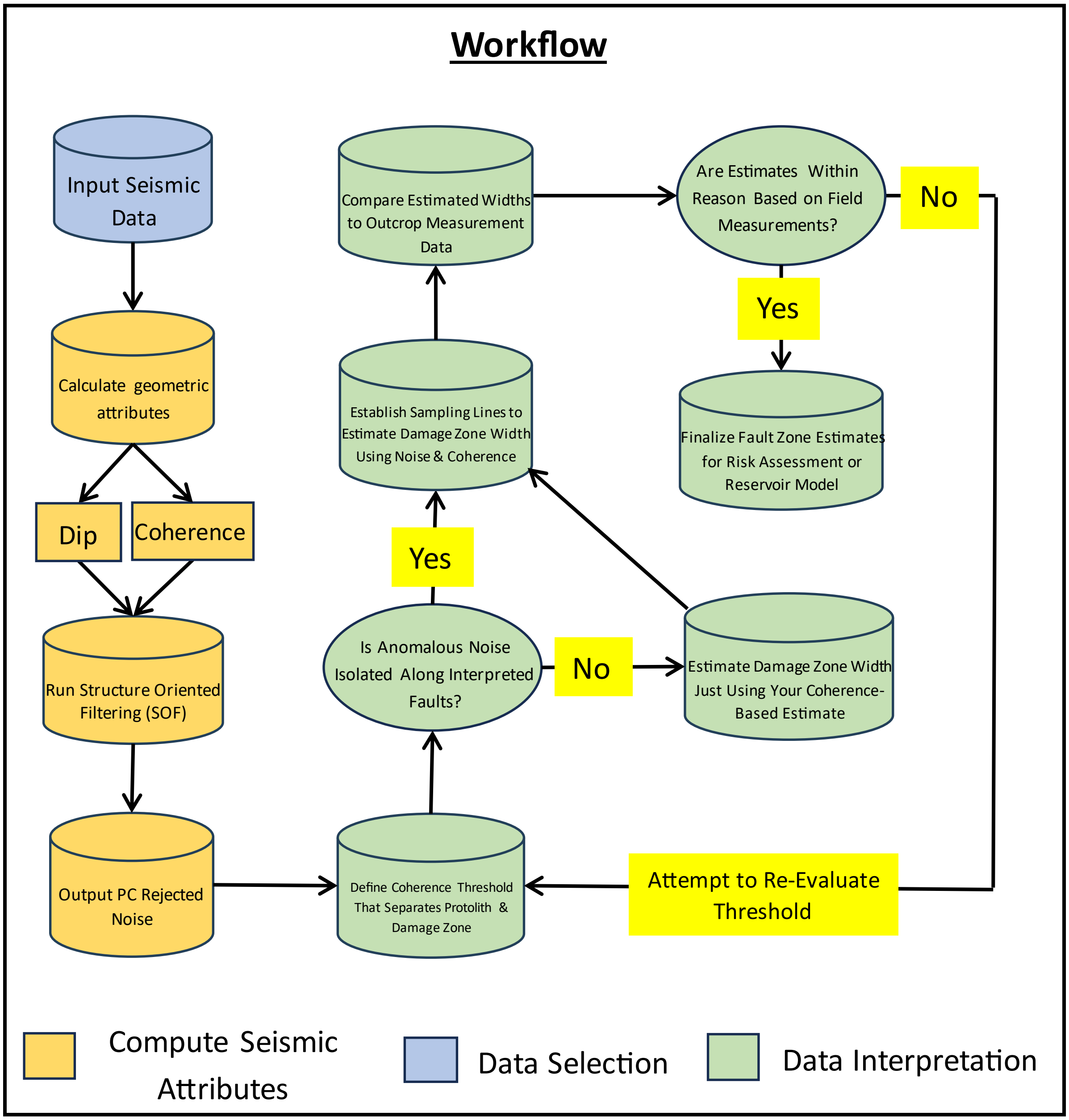

Figure 6. Workflow employed for this study. Describes method for damage zone estimates using coherence and rejected noise and what to use for validation depending on the results.

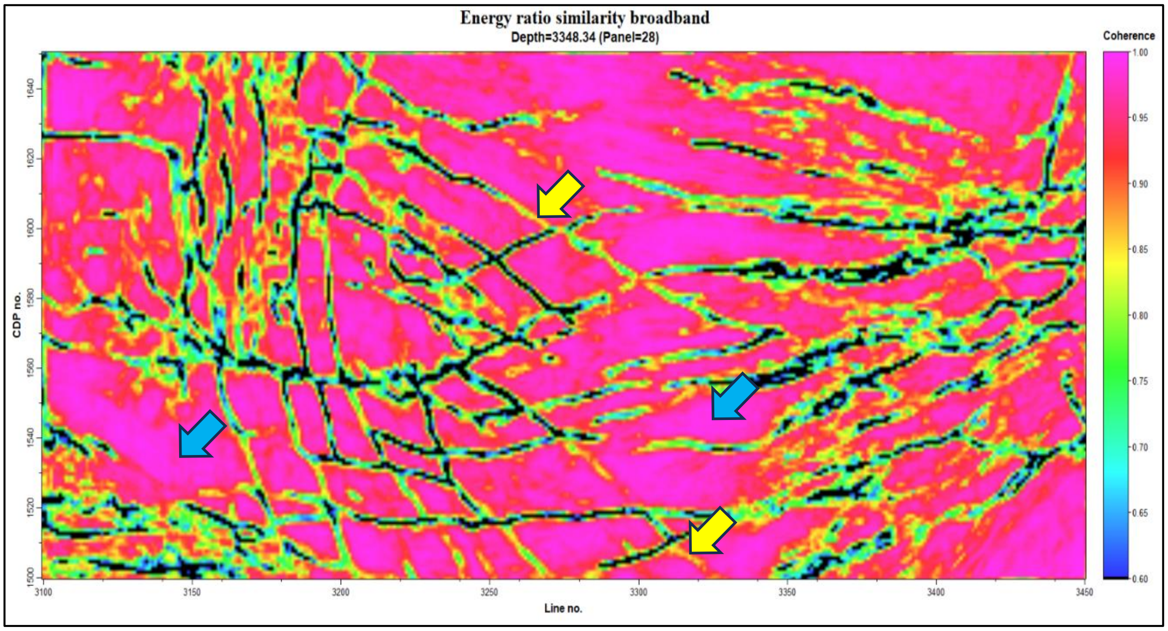

Figure 7. Energy ratio similarity depth slice in area of interest showing insight to the selection of the coherence-based threshold that marks the separation of protolith and damage zone. Yellow arrows show a well-defined segment of a fault axis with the highest observed coherence around the 0.85/0.86 range. Blue arrows are representative of protolith values which are consistently between 0.95 and 1. So the range of possible damage zone thresholds based off coherence are between 0.87 and 0.94. To fit comfortably between the upper and lower bounds, 0.9 was chosen as the benchmark that differentiates the damage zone and protolith.

Sampling Line & Fault Slip Measurements

Once the threshold coherence value was established, damage zone measurements could begin. To measure damage zone width, we established sampling lines. In this study, sampling lines, which record coherence and rejected noise values along their length, were oriented perpendicular to the strike of each studied fault's central axis. In Bacalhau, we created these sampling lines by drawing a single horizon line in Petrel perpendicular to the interpreted fault axis (Figure 8). We then extracted coherence values and the absolute magnitude of the rejected noise amplitudes along these lines and exported them as text files. Subsequently, we developed a Python script to visualize the extracted data in the form of line graphs.

To quantify damage zone width, we recorded the locations where coherence equals 0.9 on both sides of the coherence minimum representing the fault zone's center. The distance between these two points defined the modeled damage zone width using coherence. We measured estimated damage zone width for rejected noise in the same manner, using the coherence = 0.9 locations as the reference boundary. Noise was evaluated relative to the structurally defined coherence extent rather than by imposing an independent amplitude threshold, which could introduce additional interpreter bias and reduce methodological consistency between attributes. We scaled the axes for rejected noise and coherence to align with one another. We found that slight adjustments to the vertical axis maximum values had a near negligible effect on the calculated width measurements, as changing the noise axis maximum by multiples of 500 typically shift a single point's horizontal position by 0-4 meters depending on slope.

We subsequently compared coherence- and rejected noise-based fault zone width estimates to the compilation of outcrop-derived damage zone measurements presented by Savage and Brodsky (2011), which includes nearly 30 published studies in addition to their own dataset. In that study, damage zone width was analyzed as a function of fault slip. Because that study is rooted in direct field observations, it provides an independent and physically grounded benchmark for evaluating the plausibility and scaling behavior of the coherence and rejected noise-based damage zone measurements. Accordingly, we measured fault slip within the Bacalhau seismic survey to enable direct comparison with the established damage zone width-to-slip scaling relationship in field data. Figure 9 illustrates the method used to measure fault slip. We selected sampled faults to capture a wide range of slip variability within the area of interest.

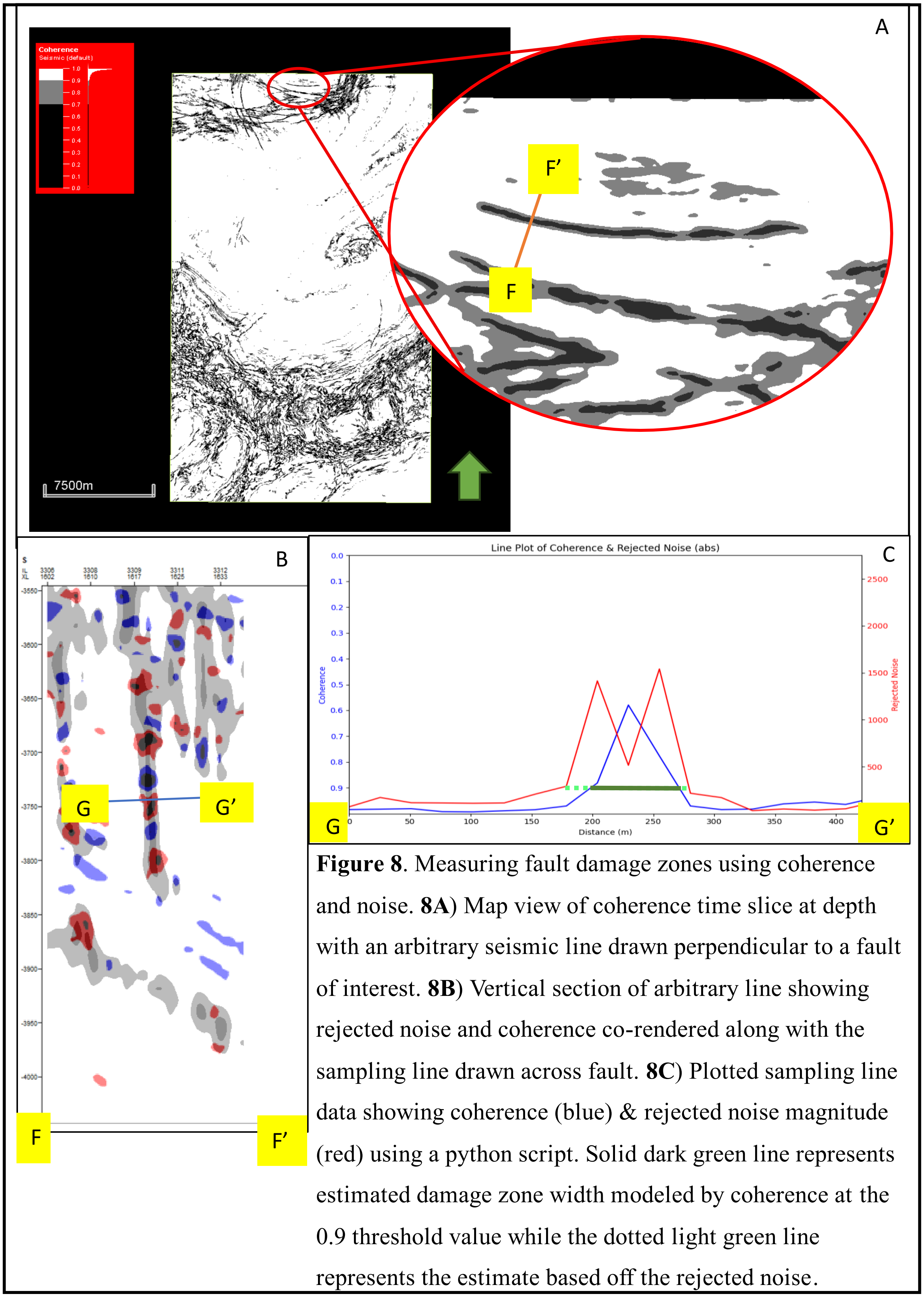

Figure 8. Measuring fault damage zones using coherence and noise. **8A**) Map view of coherence time slice at depth with an arbitrary seismic line drawn perpendicular to a fault of interest. **8B**) Vertical section of arbitrary line showing rejected noise and coherence co-rendered along with the sampling line drawn across fault. **8C**) Plotted sampling line data showing coherence (blue) & rejected noise magnitude (red) using a python script. Solid dark green line represents estimated damage zone width modeled by coherence at the 0.9 threshold value while the dotted light green line represents the estimate based off the rejected noise.

Well Data Integration

In addition to the seismic-based analysis, we incorporated two wells penetrating the Barra Velha Formation adjacent to syn-rift faults to assess rock property modification (Figure 10). Although neither well directly intersects a fault, both penetrate Barra Velha carbonates located adjacent to large-displacement syn-rift faults (>100 m throw). These carbonate intervals were expected to record fault-related alteration of rock properties through fracture development and hydrothermal fluid activity.

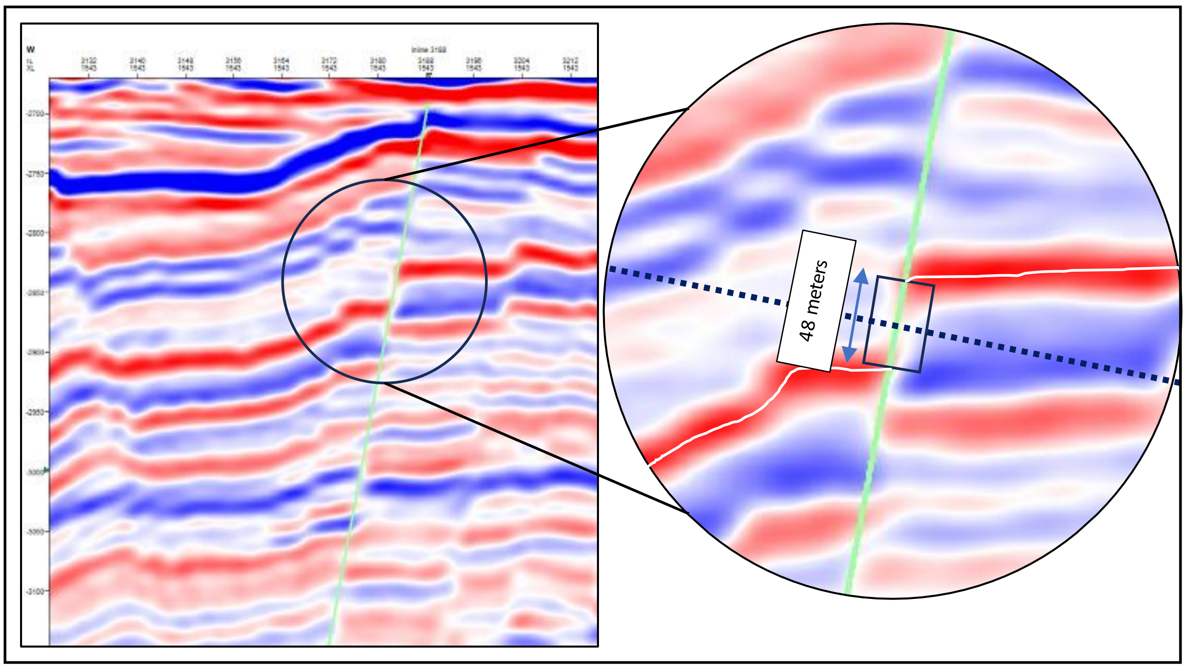

Figure 9. Fault slip measurements. Depicted above is a seismic section showing how slip is measured for each fault. Green line represents the fault plane. The white line represents the horizon for the reflector in which the slip is being recorded. The dotted black line is the direction in which the damage zone would be measured with respect to this fault segment with 48 meters of slip. Since slip measurements are done manually, it is important to express the uncertainty which was determined to be approximately 5 meters after recording the estimated slip of 3 separate fault segments with varying dips 5 different times. The damage zone to slip relationship was recorded to compare to field data measurements compiled by Savage & Brodsky (2011).

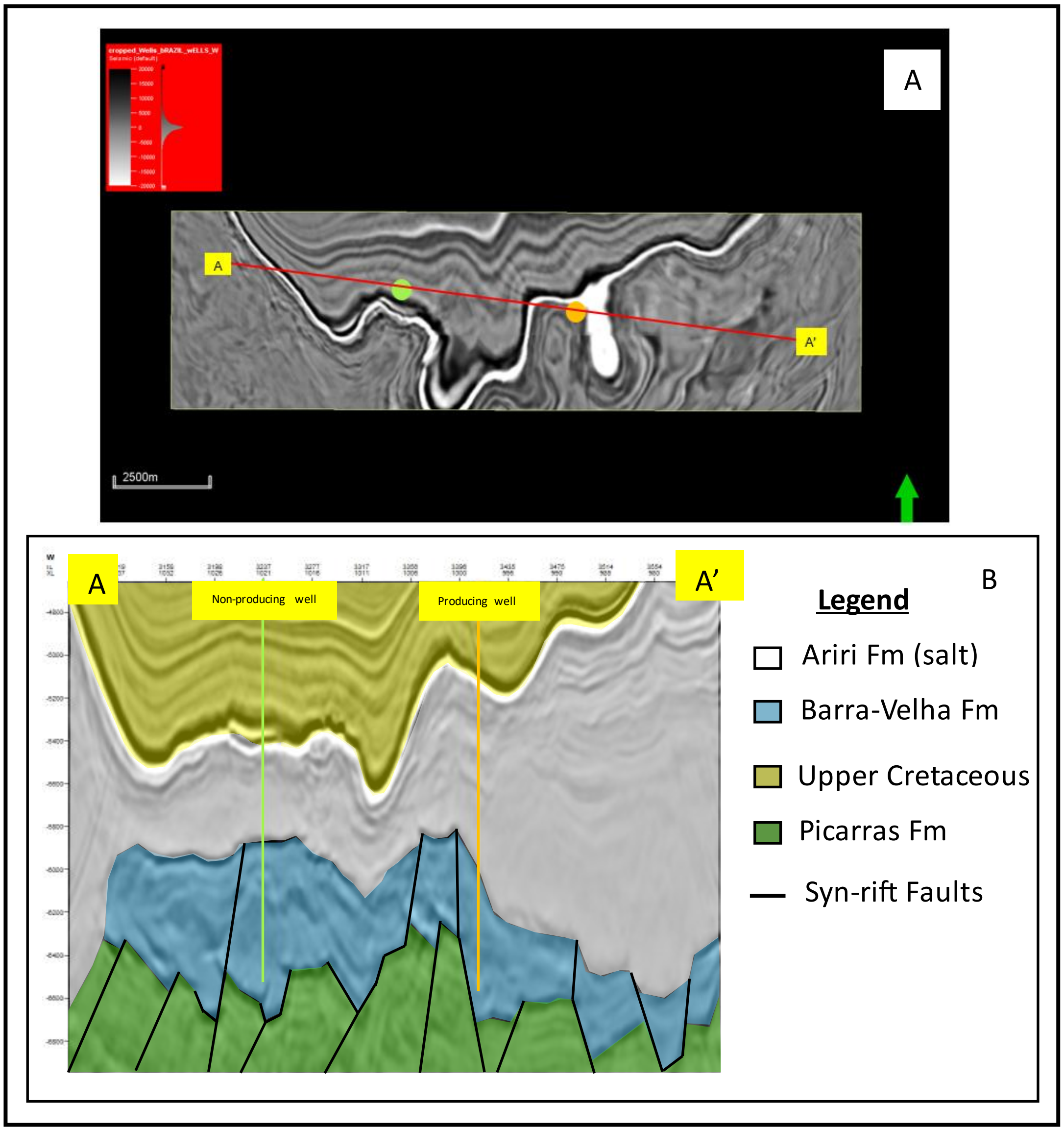

Figure 10. Bacalhau wells. **10A**) Well locations in map view showing a time slice of the seismic amplitude volume near the top of the Ariri formation with an arbitrary seismic line drawn through the wells. **10B**) Vertical seismic section of the arbitrary line co-rendered with the interpreted geology showing the well paths. These wells are approximately 13 km south of the upper Cretaceous faulted system in which damage zone widths are measured quantitatively.

This provided a separate means of evaluating the sensitivity of these attributes to fault-influenced rock properties. We extracted seismic trace data nearest to each wellbore using Petrel's 'Extract Well Seismic' function and exported these traces together with the corresponding well log data into text files. We then visualized the data using a Python script to allow direct, depth-aligned comparison of coherence and rejected noise attributes with petrophysical log responses. We used this integration to ground the seismic attribute interpretation by evaluating whether variations in noise and coherence corresponded to observable changes in rock properties at the petrophysical scale, thereby providing independent support for the use of these attributes as proxies for damage-zone characterization.

After extracting the seismic data along our wells, we used well log data, sidewall core, and conventional core reports to subdivide our wells' tested intervals into separate facies based primarily on general rock type, void space, and mechanical deformation. We then compared how rejected noise and coherence change in response to the changing facies.

To determine whether rejected noise exhibits similar behavior and remains concentrated along faults in different seismic datasets and geologic settings, we calculated SOF-derived rejected noise from two additional 3D seismic datasets. One dataset is the Matagorda mega merge, which combines two seismic surveys acquired in 1991 and 1994 on the Texas shelf; the other is the Great South Basin seismic survey acquired in 2007, offshore New Zealand. We conducted this multi-dataset comparison to evaluate whether our workflow can be repeated across different seismic volumes, and that fault generated noise isn't a phenomenon unique to Bacalhau.

Having outlined the methodological framework used to define and measure damage zone width, we now present the results of applying this workflow to the Bacalhau dataset and a noise analysis with comparative volumes. The following results section evaluates coherence and rejected noise damage zone estimates, compares how they align with fault zone envelopes based on field measurements, as well as their consistency with well logs and core data.

RESULTS

Qualitative Analysis of Rejected Noise & Coherence

The first step was to analyze the rejected noise and coherence for comparison. In Bacalhau, coherence was more reliable overall when it came to mapping fault damage zones when compared to the rejected noise. The reason for this was attribute continuity. Coherence anomalies that are aligned with interpreted faults do not alternate between background values and damage zone values along the fault plane. Rejected noise is more erratic in this regard, presenting itself as tightly grouped pockets of high magnitude values rather than a continuous anomaly along fault zones. Coherence lows were consistently aligned along interpreted faults and only became variable in certain areas where reflectors were erratic, possibly due to low signal-to-noise ratio. Rejected noise anomalies were abundant in structurally coherent areas and often mimicked seismic stratigraphy, as the anomalies were vertically stacked, elongate, and parallel to reflector dip. Attempts to mitigate this noise were made by adjusting analysis window parameters and coherence thresholds, but neither made a noticeable difference in how the noise presented itself in this dataset.

While anomalous noise was prevalent in regions with no interpreted faults, the morphology of how the noise presented itself along structural discontinuities was noticeably different compared to how noise appeared when it resembled seismic stratigraphy. Along fault zones, rejected noise presented itself as nodular, severely misshapen, or vertically elongate non-parallel to dip. Rejected noise appeared in this same way along interpreted small-offset faults that did not register a coherence anomaly and showed better continuity along faults than coherence in certain regions. This is plausible given previous studies that have identified alternate seismic attributes that can visualize small-offset faults that don't exhibit a coherence anomaly such as aberrancy, the derivative of the seismic attribute curvature (Qi & Marfurt, 2018). Additionally, misshapen noise anomalies showed a connective nature between closely spaced faults (typically less than 250 meters of horizontal separation) in certain regions. These instances where the rejected noise makes fault interpretations more robust in Bacalhau are shown in a crossline 1577 (Figure 11). While other data types such as well or core data would be needed to corroborate whether this is highlighting deformation that is below seismic resolution, it introduces a new way to risk potentially fractured intervals in the early stages of well planning and in the assessments of seal rock integrity.

Figure 12 presents vertical seismic sections from the Matagorda and Great South Basin (GSB) datasets, with seismic amplitude co-rendered with SOF-derived rejected noise, illustrating anomalous noise concentrations along interpreted faults similar to those observed in Bacalhau. Although both secondary datasets contained intervals where noise was aligned parallel to dip and not proximal to structural offsets, rejected noise was generally more concentrated along interpreted faults than in Bacalhau. Because anomalous noise aligned with faults was observed across all datasets, this behavior does not appear to be unique to Bacalhau, suggesting that the workflow is repeatable across other 3D seismic surveys.

Rejected noise produced by SOF contains a mixture of signal types, and not all anomalous noise is structurally driven. In practice, we observed two recurring noise morphologies: (1) irregular, nodular, and vertically elongate noise that is spatially aligned with interpreted fault planes and concentrated near structural offsets, and (2) smoother, laterally continuous noise that is dip-parallel and tracks seismic stratigraphy character, even where structural offset is absent. Because these two noise expressions carry different interpretive meaning, we developed a classification scheme to separate fault-zone–related noise from stratigraphy-mimicking noise prior to estimating damage zone width. For the purposes of this study, we classified noise aligned with fault geometry and structural discontinuities as **Type A** (fault-zone related), and noise that follows stratigraphic behavior without clear structural association as **Type B** (non–fault-zone related).

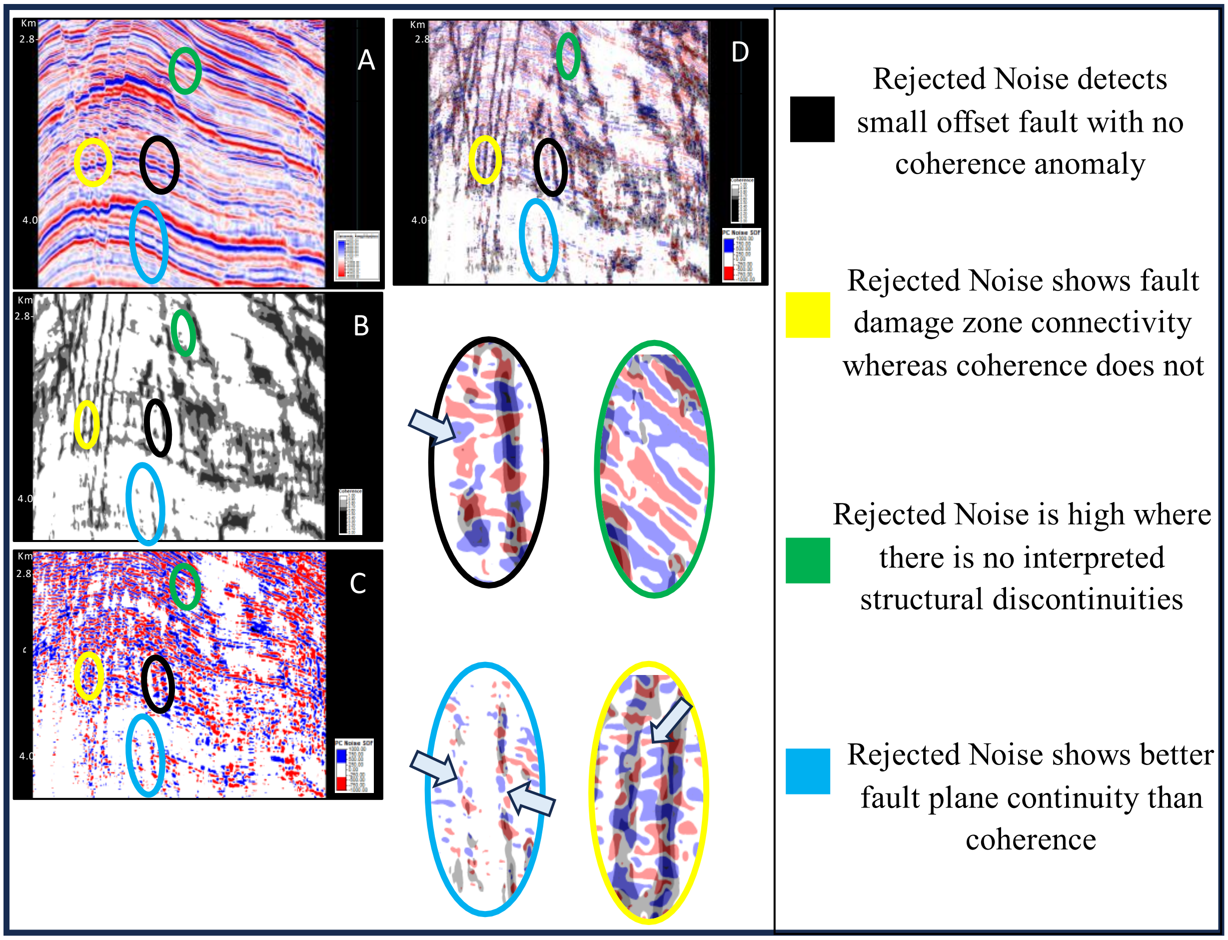

Figure 11. Bacalhau data from 1577 crossline section. **11A**) seismic amplitude data **11B**) energy ratio similarity/coherence **11C**) rejected noise **11D**) rejected noise and coherence co-rendered. Circled regions (except green) highlight best examples on the crossline of regions where the rejected noise improved fault interpretability (blue & black) or added nuance to existing fault zone architecture (yellow showing potential damage zone connectivity).

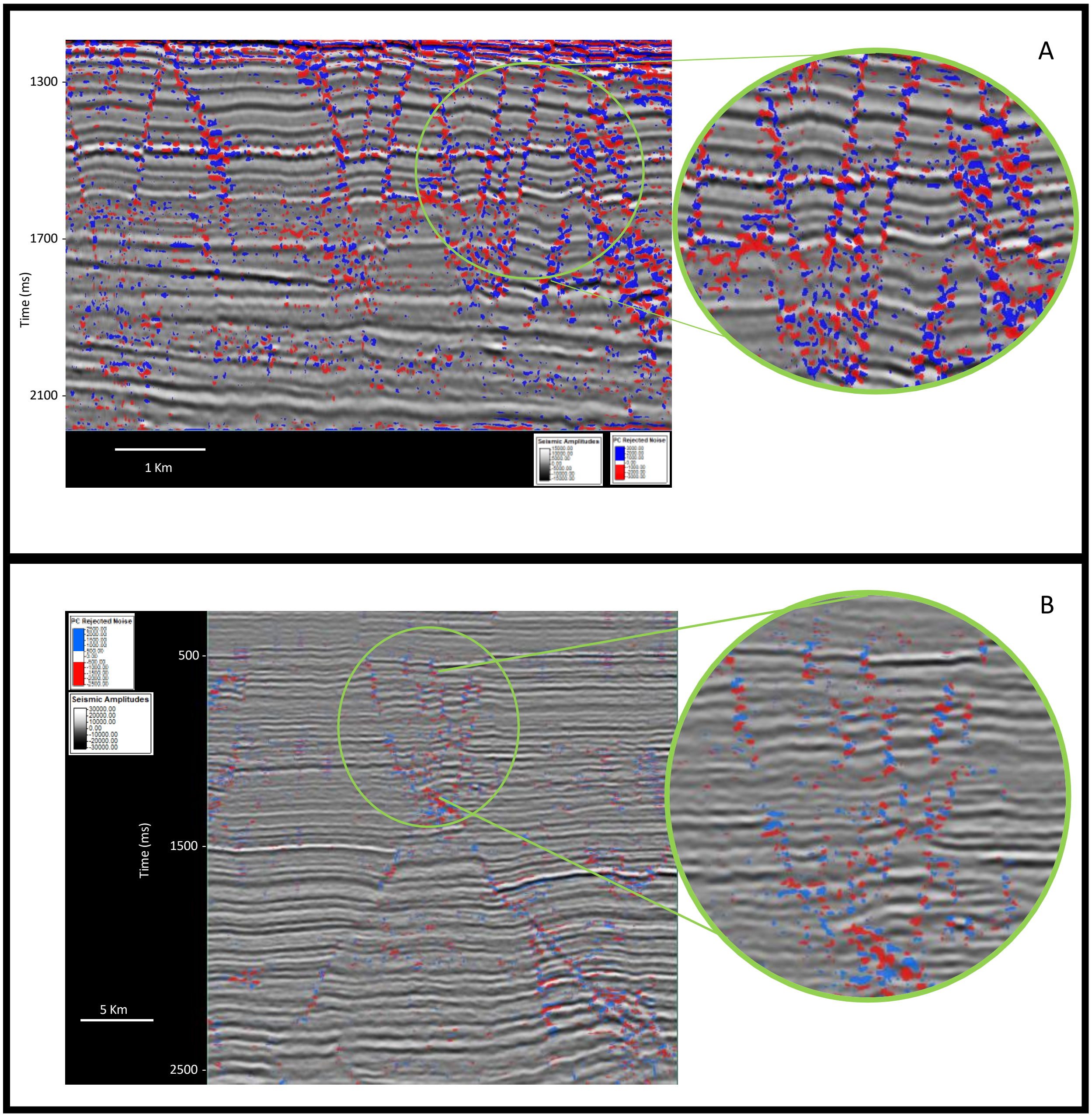

Figure 12. Noise co-rendered with seismic amplitude data in other datasets. **12A)** Vertical seismic section showing amplitude and rejected noise data within a polygonal fault system in the Great South Basin, offshore New Zealand. **12B)** Seismic amplitude and noise data near the Clemente-Tomas fault zone, Gulf of Mexico. Prevalence of anomalous noise along faults in multiple seismic datasets shows that our proposed workflow can be repeated across different seismic datasets. The noise classification scheme introduced in this study is applicable as Type A noise (misshapen, nodulus, or vertically elongate along structure) and Type B noise (elongate and parallel to stratigraphy) is prevalent in both secondary datasets.

Damage Zone Width Estimates

When quantifying damage zones using the sampling line method, we avoided using rejected noise as a measuring tool when Type B noise was directly adjacent to the fault zone being measured. This would skew interpreted damage zone widths derived from rejected noise and be prone to overestimation. A representative example in which it was appropriate to quantify a fault zone using both noise and coherence using the sampling line method is shown in Figure 8B, where Type B noise is low magnitude away the fault, and Type A noise is high magnitude and aligned well with the coherence anomaly that represents the fault zone. Fault zone widths can still be estimated in the presence of Type B noise; however, this would likely require a type of polygon-based extraction in which the interpreter manually delineates fault zone boundaries based on the morphology of Type A noise that consistently aligns interpreted faults.

In Figure 13, we plotted damage zone width estimates based on sampling line data for both rejected noise and coherence as a function of fault slip. There was a strong linear correlation between coherence-derived width and slip, whereas rejected noise-derived widths were more variable. This was quantified by calculating the residual standard error (RSE) and R^2 of the best fit line for coherence and rejected noise. The coherence-derived regression yielded an R^2 of 0.64 and a RSE of 16.4 m, indicating higher explanatory power and relatively constrained scaling relationship. In contrast, the rejected noise regression exhibited a markedly lower R^2 of 0.035 and a substantially higher residual standard error of 47.2 m, reflecting weaker explanatory power and significantly greater scatter.

The most common difference between noise and coherence-derived damage zone widths was approximately 20–30 meters, accounting for roughly two-thirds of the sampling lines where both measurements were taken. The remaining one-third exhibited substantially larger discrepancies, with differences in width of at least 75 meters.

Comparison of our coherence-derived damage zone width measurements with the field compilation of Savage and Brodsky (2011) showed that our coherence data fell within the scatter of displacement–damage zone thickness data points recorded in field studies by various authors (Figure 14). Across the analyzed range of slip values, our coherence measurements followed a comparable scaling trend—approximately a 1:1 ratio as the measured slope of the best fit line was 0.998. In the field dataset compilation, this growth pattern continued until displacement exceeded 1000 meters, after which damage zone growth tapered.

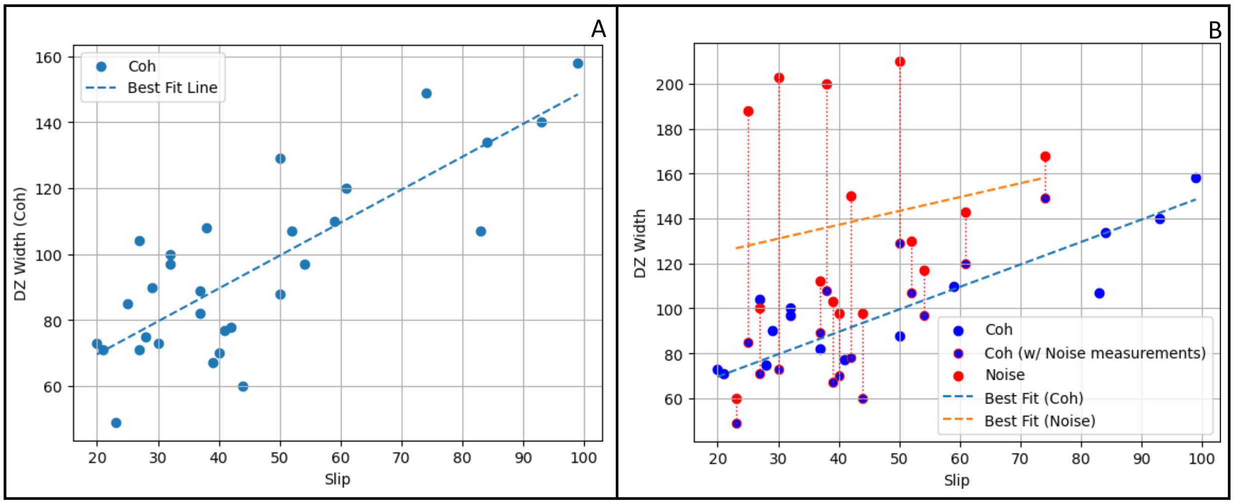

Figure 13. Scatter plot of sampling line measurements. **13A**) Damage zone (DZ) width estimated from coherence (Coh) plotted against measured fault slip with a line of best fit. **13B**) Rejected noise co-rendered with their corresponding coherence data points and their respective lines of best fit. Noise was only recorded with coherence along faults with minimal Type B noise.

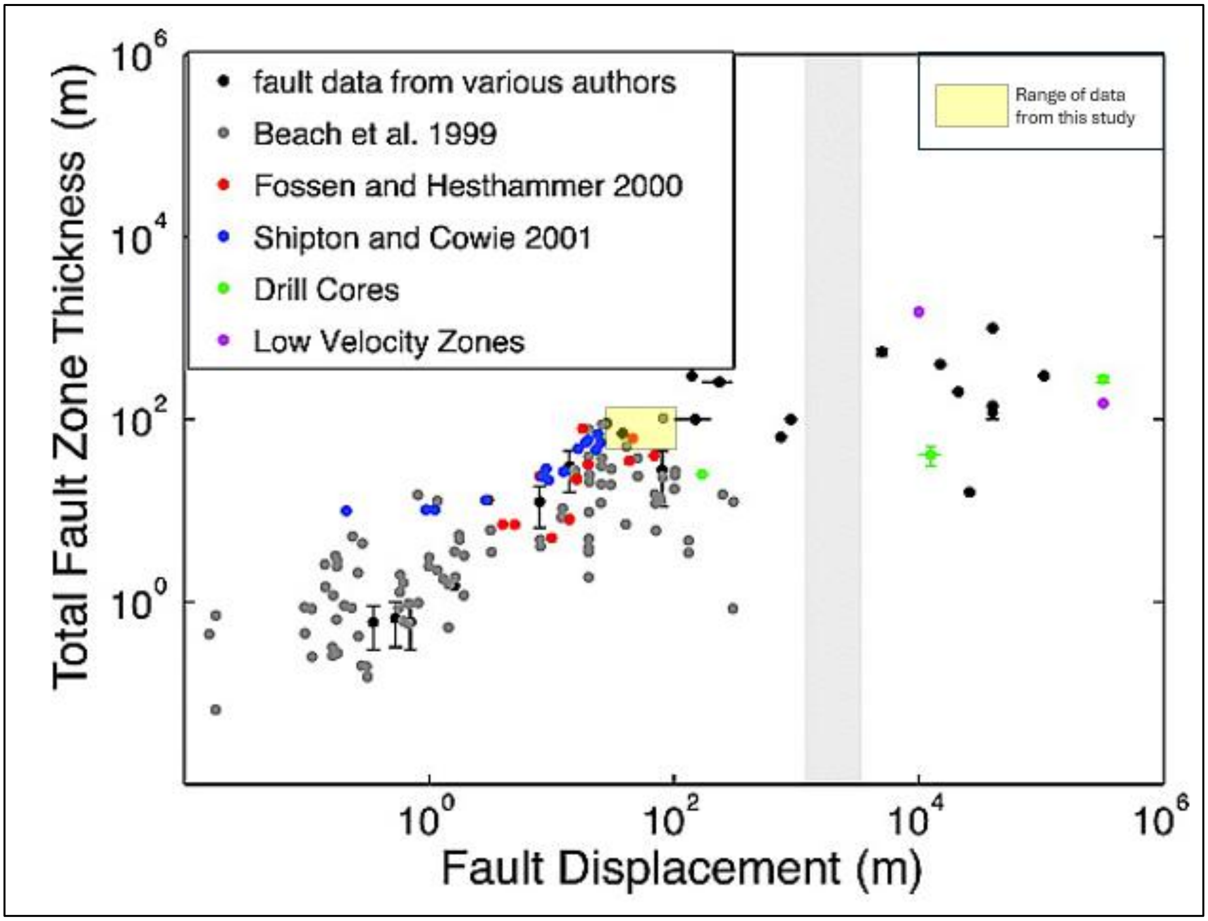

Figure 14. Coherence-based estimates co-rendered with field data gathered from various authors. Vertical gray stripe represents the threshold where damage zone growth appears to stop increasing with fault displacement around 1000 meters of slip and above. From 0 to 1000 meters, the overall trend of the data can be represented by a 1:1 ratio with a range of substantial scatter. Modified from Savage & Brodsky (2011).

Well Data Findings

For the productive well in Bacalhau, we subdivided the tested interval into five facies based on well logs, sidewall core, and conventional core descriptions. Apparent porosity and the presence of fractures were explicitly documented in the core reports, and we used these metrics as the basis for facies classification. This approach was adopted to emphasize mechanical deformation (fracture development) and void space. In this dataset, void space is in part represented by apparent porosity; however, in other structural settings, void space may also be accommodated by open fractures. Although matrix porosity is not necessarily a direct function of fault processes in this case, we included it to account for total void space within the interval. Rocks that showed little to no intervals of mentioned apparent porosity or fractures and had RHOB values that were higher comparatively to the surrounding intervals were given a classification of "tight." The well log data, extracted noise and coherence values along the well, and facies classifications, are all depicted together in Figure 15.

Coherence was most sensitive within the altered carbonate interval characterized by elevated fracturing and apparent porosity. In contrast, rejected noise showed highest sensitivity at the interface between tight, to porous and fragmented volcanics/volcaniclastic rocks. This boundary also corresponded to the largest decrease in RHOB observed along the well log. Notably, coherence values at this interval remain near 1, indicating no response in the coherence volume. This contrast highlighted the complementary behavior of the two attributes and demonstrated that rejected noise captures significant petrophysical transitions that coherence does not resolve, supporting its use as an independent seismic attribute with the potential for substantive interpretable use.

For the non-productive well there was limited available well log data. RHOB was most noticeably absent, so we gave rocks a tight classification for having dominantly no apparent porosity or fractures mentioned in the core reports. This does introduce a higher degree of uncertainty in the facies classifications, especially when compared to the productive well. The well logs, facies classification and extracted noise/coherence values along the well are displayed in the same manner as they were for the productive well in Figure 16.

Coherence exhibited a modest spike at the transition from porous volcaniclastic rocks into overlying tight volcanic and volcaniclastic units. In contrast, rejected noise displayed its largest spike at the salt–carbonate interface and a secondary peak at the transition from tight carbonates into porous, fractured volcanic and volcaniclastic rocks. The decrease in coherence near the base of the well suggests proximity to a potentially fractured interval; however, no reflector offset is observed beneath the well to indicate faulting. At depths exceeding 6 km, the vertical resolution of the seismic data limited our ability to resolve subtle structural discontinuities, restricting fault interpretations primarily to the large syn-rift basement faults, which need a vertical offset of at least 50 meters in order to be resolved in the regions around the tested well intervals.

The anomalous noise at the start of the log is attributed to the strong impedance contrast between salt and carbonate and is morphologically consistent with Type B noise as opposed to being related to structural deformation more likely associated with Type A noise. The most significant petrophysical change occurred at the second highest rejected noise peak, where it captures the transition from tight carbonates to porous, fractured volcanic and volcaniclastic rocks, which coincides with a pronounced increase in NPHI observed in the well log. The morphology of the noise here is more consistent with Type A noise, as it did not mimic the seismic reflector in which it resides. This again provides further evidence that rejected noise responds more strongly to rock property changes than coherence, justifying the value in its use for interpretive workflows in seismic data.

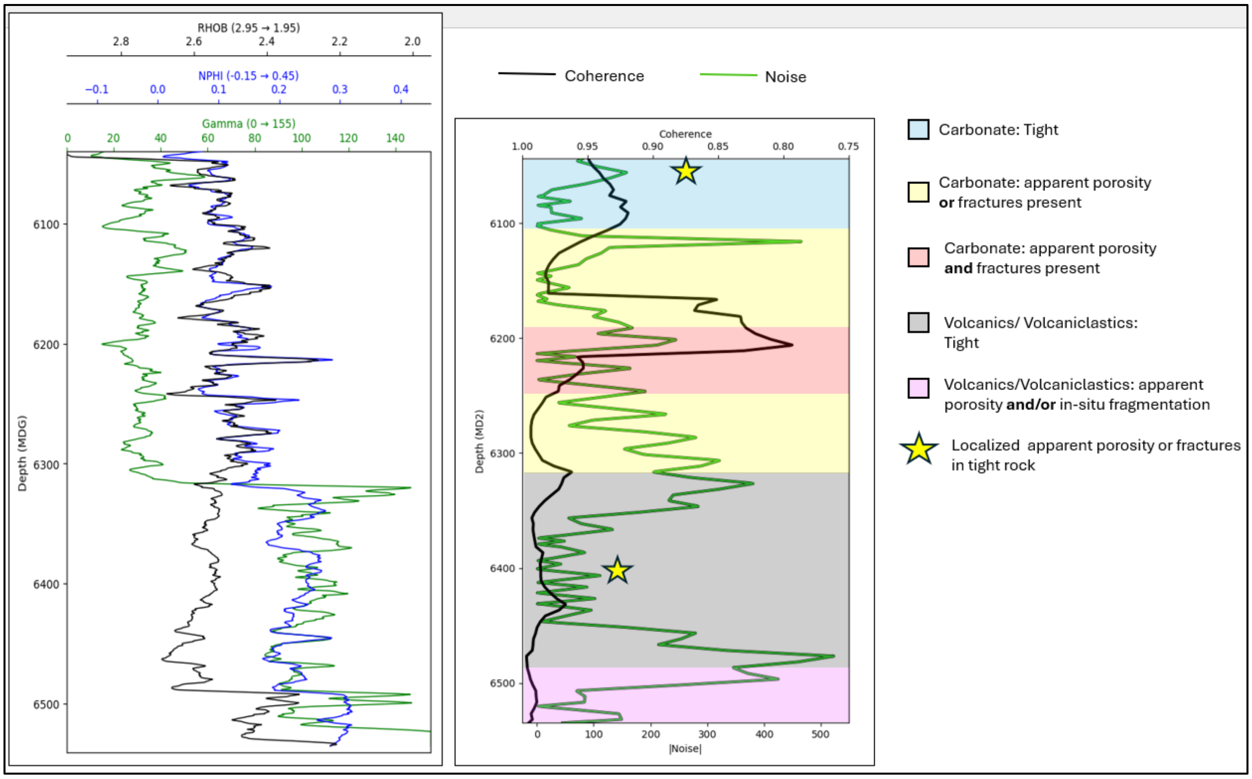

Figure 15. Log and seismic data for the productive well. The well log data was formatted to look like a triple combo, where Gamma, RHOB, and NPHI show increasing shale content, lower bulk density and increasing hydrogen moving towards the right respectively. The coherence and rejected noise magnitudes were extracted along the well and are co-rendered with a color-coded facies interpreted from sidewall and conventional core data. The labels of the facies are meant to highlight void space indicated from apparent porosity and mechanical deformation. Coherence captures the interval with the best reservoir properties in the red facies, while the rejected noise captures the changes in petrophysical properties at multiple interfaces along the well that exhibit background or decreasing coherence values.

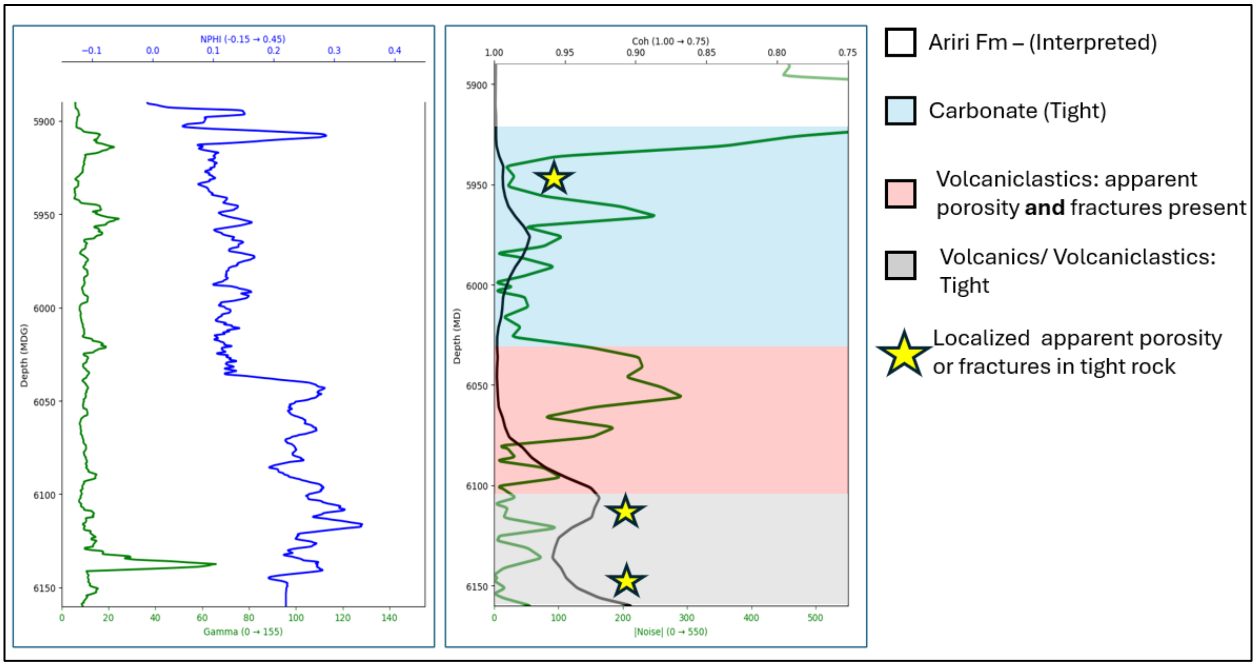

Figure 16. Log and seismic data for the non-productive well. The well log data available was Gamma and NPHI which show increasing shale content and increasing hydrogen moving towards the right respectively. The absence of other well logs is likely because the well was non-productive. Similar to Figure 15, the coherence and rejected noise magnitudes were extracted along the well and are co-rendered with a color-coded facies interpreted from sidewall and conventional core data. The labels of the facies are meant to highlight void space and mechanical deformation. Since no RHOB was present, intervals are assumed to be "tight" if fractures or apparent porosity are not a dominant characteristic of the interval. This does introduce more uncertainty in the facies classification compared to the productive well.

The major findings of this study thus far indicate that rejected noise exhibits a noticeably different morphology along faults compared to continuous stratigraphy, that the scaling relationship between damage zone width and fault slip estimated using coherence shows a trend similar to field data, and that rejected noise is particularly effective at identifying facies changes in the wells compared to coherence. We explore each of these ideas in greater depth, along with their implications for exploration and risk analysis, in the discussion section below.

DISCUSSION

Noise Morphology

The goal of this study was to evaluate whether coherence and noise removed by structure-oriented filtering (SOF) could be used to produce more robust fault zone characterizations. A primary challenge in the Bacalhau dataset was the abundance of stratigraphy-mimicking noise, which made morphological distinction essential for separating structurally meaningful anomalies from high amplitude variability in structurally continuous rock. The recurrence of this morphological distinction in two additional seismic datasets from different basins (Figure 12) suggests that the workflow may be generalizable and applicable across a broad range of seismic datasets.

An important consideration is the abundance of Type B noise within a given dataset. Frequency content likely exerts significant control. In the region where damage zones of multiple Upper Cretaceous faults were quantified (Figure 11), the vertical resolution was approximately 10 meters, which is relatively high frequency for offshore 3D seismic surveys. With increasing depth, the occurrence of Type B noise diminished. This reduction is likely related to progressive attenuation of high-frequency seismic energy. As seismic waves propagate to greater depths, attenuation of higher frequencies results in a broader wavelet and reduced vertical resolution. This reduction in bandwidth suppresses small-scale lateral and vertical variability within the seismic data, producing reflectors that appear smoother and more laterally uniform within the SOF analysis window.

Because the filtering approach employed in this study retains the first principal component as the representative signal, reduced amplitude variability at depth allows this dominant component to capture a larger proportion of the total variance. Consequently, the residual energy—expressed as Type B noise—decreases as complexity within the analysis window is dampened. In contrast, larger-scale structural discontinuities associated with faulting remain resolvable despite bandwidth loss, preserving the relative prominence of Type A noise anomalies at greater depths.

The distinct morphology of noise aligned with faults can also be interpreted within this filtering framework. In structurally continuous regions with high signal-to-noise ratio, the dominant direction of variance within the analysis window is spatially stable. This may explain why Type B noise appears planar and maintains consistent orientation along reflectors. In contrast, where structural discontinuities are present and signal-to-noise ratio is reduced, the dominant variance direction becomes less stable spatially. This instability likely contributes to the nodular or irregular character of noise anomalies observed adjacent to interpreted faults, reflecting more abrupt changes in local variance structure.

Sampling Line Data

Rejected noise consistently yielded wider damage zone estimates than coherence along each sampling line as shown in Figure 13. Noise was more difficult to measure along faults compared to coherence because it was less consistently confined to structural discontinuities. The presence of Type B noise adjacent to faults could artificially inflate estimated damage zone widths; therefore, rejected noise was recorded only where there was high confidence that Type B noise was not prevalent in the surrounding area.

For most data points where both coherence and rejected noise were measured, noise yielded damage zone widths approximately 20–30 meters greater than those derived from coherence. In these cases, the noise attribute did not detect structural features that coherence failed to identify; instead, it produced wider estimates because it naturally has a higher range compared to coherence. Noise amplitudes can increase from tens to thousands when entering a fault zone, whereas coherence is limited to a 0–1 scale. As a result, the wider widths often reflect the steeper amplitude gradient of noise approaching interpreted fault zones compared to the nonlinear decrease observed in coherence even after the coherence and rejected noise axes were scaled to match one another.

There were five instances in which noise-based widths exceeded coherence-based widths by at least 75 meters, three of which differed by more than 100 meters. In these cases, the discrepancy could not be explained solely by slope differences; rather, the noise amplitudes increased more rapidly and remained elevated over a broader spatial interval than coherence. One measured fault segment exhibited a noise-derived damage zone width of 188 meters despite a slip of approximately 26 meters. A damage zone of this size is unlikely for a fault with such limited displacement. A more plausible explanation is that the noise attribute could be responding to subsidiary faults and their respective damage zones are connective. This type of phenomenon would fall below seismic resolution. The seismic section showing where this measurement was taken is depicted in Figure 17, where the damage zone envelopes modeled by coherence and the rejected noise are outlined separately.

This interpretation remains speculative and would require additional data for confirmation; however, preliminary observations from well data provide some support for this possibility and are discussed in following sections.

Another pattern observed in several sampling lines was a sudden decrease in rejected noise within the interpreted center of the fault zone, coincident with the coherence minimum (Figure 8C). This behavior may be related to the filtering algorithm, which employs overlapping analysis windows to avoid filtering seismic traces associated with the lowest coherence values. It may also result from reflector offset, as this phenomenon appeared more prevalent along faults exhibiting greater slip.

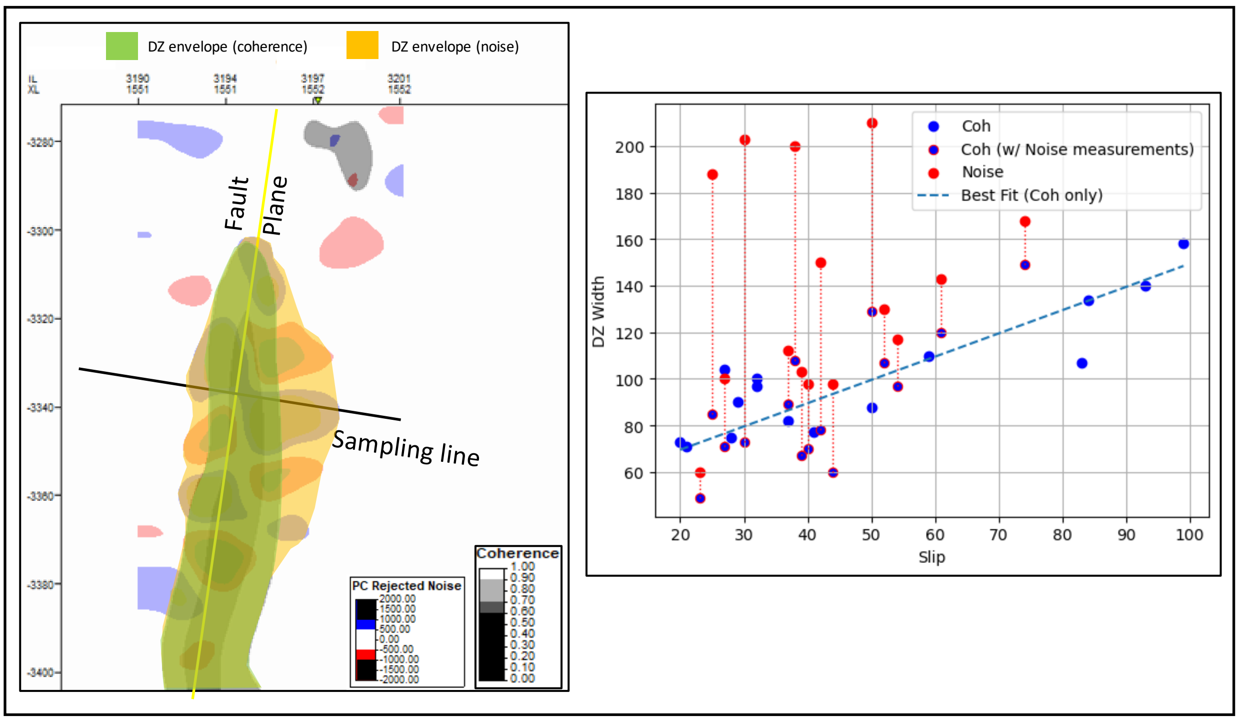

Figure 17. Sampling line example where noise shows a considerably wider damage zone than coherence. Sampling line being depicted is black. Coherence is co-rendered with rejected noise in the fault perpendicular arbitrary section pictured on the far left where the fault plane and sampling line were created. The orange polygon represents the damage zone envelope represented by the rejected noise while the coherence-based envelope is represented by the green polygon.

Fracture density is commonly described as following an approximately exponential decrease with distance from the fault core, such that fracture intensity diminishes rapidly away from the core zone (Xing et al., 2022; Savage & Brodsky, 2011; Ostermeijer et al., 2020). The coherence and rejected noise profiles along our sampling lines exhibited a similarly sharp, nonlinear decrease with increasing distance from the fault center. In Figure 18, we interpreted the fault core as being centered around the coherence minimum for each sampling line. We can observe the same exponential-like / nonlinear rapid decrease in coherence values as we move away from the interpreted fault center. Noise does not follow this same manner as cleanly as coherence, because noise dampens around the interpreted fault core for reasons previously discussed.

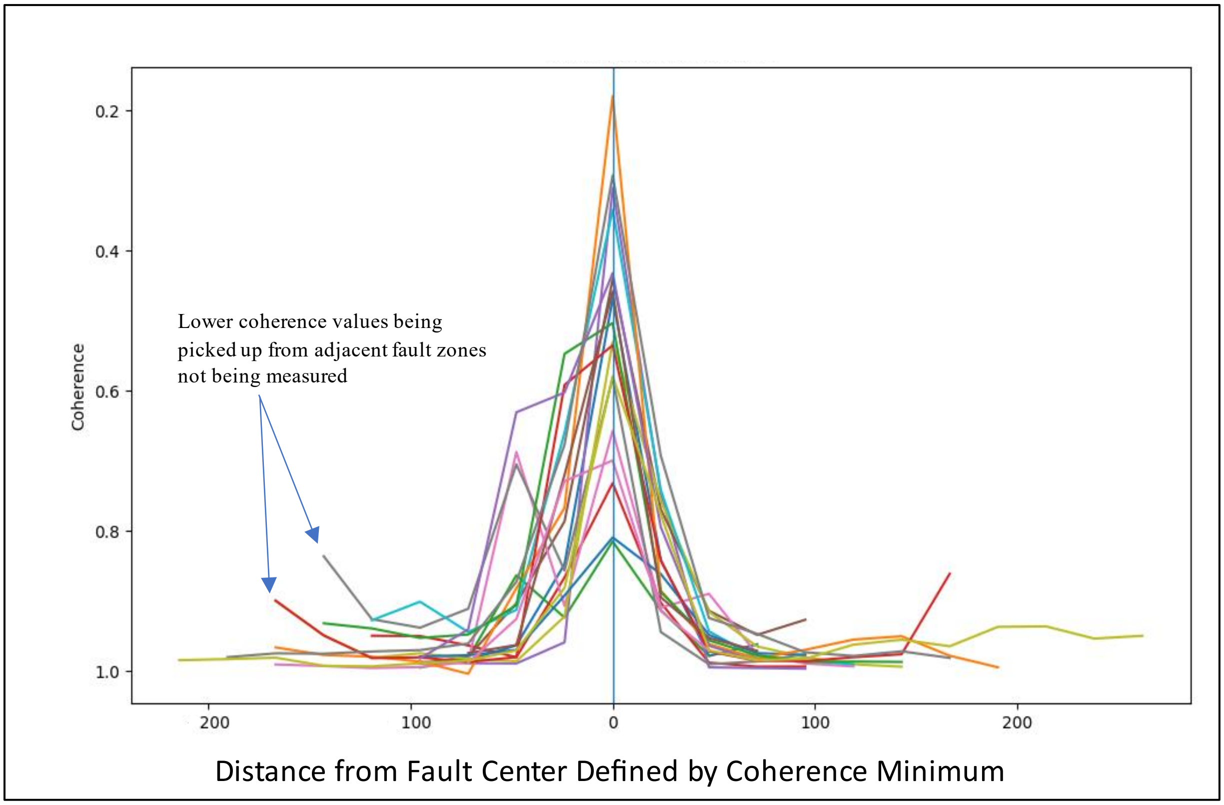

Figure 18. Coherence values along sampling lines. We interpreted the coherence low for each sampling line to represent the center of each respective fault zone. Coherence displays the same positive exponential behavior as distance to the fault zone's center decreases in the same way that fracture density increases at roughly an exponential rate as distance to the fault core decreases as documented throughout many field studies. Some sampling lines picked up lower coherence values due to proximal faults zones that weren't being measured.

Outcrop Data Comparison

Savage and Brodsky (2011) observed an approximately 1:1 relationship between fault slip and damage zone width, with a substantial scatter for slip values between 0 and 1,000 meters. Beyond approximately 1,000 meters of slip, damage zone width ceased to increase proportionally with displacement and tapered (Figure 14). Our study had a more limited range comparatively, as faults with slip less than approximately 10 meters cannot be resolved in the seismic data. The smallest slip recorded was 20 meters and the largest was 99 meters.

The line of best fit for slip vs damage zone width derived from the coherence data in Figure 13 was:

$$y = 0.9983x + 49.6428$$

where y represents damage zone width and x represents slip. Because slip measurements are limited to 20 meters and above due to seismic resolution, the y-intercept is likely biased high. Extrapolation of the approximate slip = damage zone width trend suggests it may be closer to ~30 meters. The near 1:1 slope indicated strong agreement with the scaling relationship documented in outcrop studies.

The interpreted intercept adjustment to ~30 meters suggested that damage zone widths may be overestimated by approximately this amount on average. However, this overestimate is likely smaller than calculated. Slip values derived from seismic data are typically underestimates of true fault displacement, as only dip-slip components can be measured and any oblique slip component is not captured. When this limitation is considered, the coherence-derived scaling relationship would be closer to the primary width–slip trend observed in field data of a 1:1 ratio.

Unfiltered Coherence vs. Filtered Coherence

Coherence is often employed in interpretation workflows and applied to seismic amplitude data after it is has already undergone SOF. In this study we chose to compare the coherence and rejected noise calculated from the raw seismic amplitude data because we determined that comparing the rejected noise to the coherence derived from SOF amplitude data would bias the rejected noise to estimate much wider damage zones than coherence. Nevertheless, we did still examine both coherence volumes for comparison and the coherence from the SOF filtered data affected damage zones widths by a wide variability, decreasing damage zone width estimations anywhere from 5 to 60 meters in certain areas.

In practice, the filtered data would likely bring the results closer to the general 1:1 damage zone to fault slip relationship observed in field studies, however, it is important to note that this relationship represents a general trend, with some faults consistently plotting above or below it. Additionally, as it pertains to risk assessment, overestimating the extent of a damage zone with respect to planning for drilling hazards or seal rock characterizations is more preferable compared to underestimating total damage zone width. The opposite is true in cases where damage zones are the main control on reservoir permeability.

The purpose of this study was to highlight the potential geologic value in noise. While coherence has shown to be more consistent in fault zone mapping and more comparable to field-based trends than SOF derived rejected noise, coherence will naturally have some embedded noise unless it is calculated on filtered amplitude data. Since interpreters tend to use coherence in their analysis only after they have conditioned their seismic amplitude data, could they be potentially missing out on useful information hosted within in the original amplitude data? To test this, we compared the differences in coherence values derived from the original and filtered seismic amplitude data along the fractured and porous carbonate interval in the productive Bacalhau well. The results are shown in Figure 19 by showing what the productive carbonate interval looks like in a vertical section showing the coherence values on the filtered vs. unfiltered data.

Not only does rejected noise show better sensitivity at rock interfaces than coherence, but the only coherence anomaly that is centered about the fractured and porous carbonate section of the Barra Velha on the productive well only identifies that significant interval because of the noise embedded with the coherence attribute. If similar instances of this phenomenon become apparent in different datasets, it could fundamentally change how seismic noise is treated in interpretation workflows.

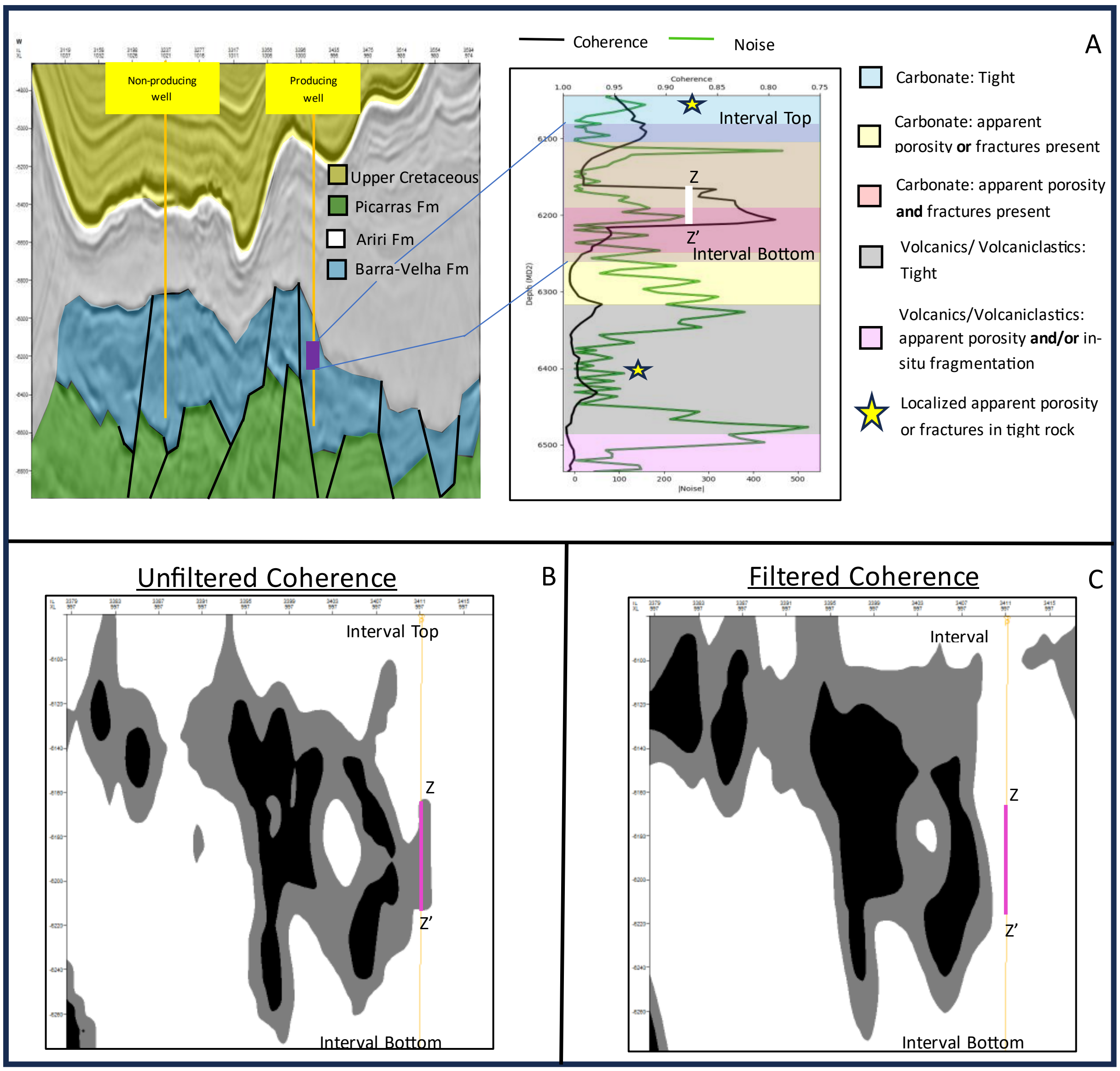

Figure 19. Comparison of coherence derived from raw seismic amplitude volume vs. coherence derived from SOF amplitude volume. **19A)** vertical seismic amplitude section showing the wells and the interval studied being highlighted by the purple rectangle. This rectangle is further visualized in our graph showing the facies classifications along with the corresponding coherence and rejected noise values extracted along the productive well. The coherence interval that shows the high-grade reservoir carbonates is denoted by Z – Z'. **19B)** Vertical unfiltered coherence section that is depicted from the purple rectangle in 19A. Coherence in this volume shows an anomalous response to the high graded reservoir interval. **19C)** Vertical filtered coherence section showing the same region. Coherence in this volume does not show an anomalous response to the high graded carbonate interval. Given these circumstances, the embedded noise within the unfiltered coherence volume was able to accurately identify the most productive interval of the carbonate reservoir, whereas the filtered coherence volume was reduced to background/protolith values over the same interval.

Bacalhau Well Data

As mentioned above, the rejected noise appeared to have captured more detail at the petrophysical level than coherence. In Figure 19A, the rejected noise reaches its second-highest magnitude at the interface between tight carbonates and fractured or porous carbonates, whereas coherence exhibits a sharp decrease, contrary to what would be expected at that interface. The largest coherence increase was directly associated with the most productive section of the well where there was apparent porosity and significant fracturing, some of which was associated with hydrothermal alteration and silicification reported in the core logs along that interval. Noise had a small increase there that aligned with the coherence anomaly but was not significant enough to be considered anomalous. This matched the same scenario mentioned earlier in which noise tended to dampen where coherence was the lowest. This relationship highlighted how the rejected noise and coherence were meant to complement one another instead of one being heavily weighted over the other. The interface between the carbonate and volcaniclastic facies was best highlighted by the rejected noise, with its third highest spike at that interval. There was a slight inflection in the coherence but not enough to be counted as anomalous due to the fact that it reached 0.96 at its lowest, which was considered a background value for the volume. Noise values remained consistently low within the tight volcaniclastic facies until a pronounced spike occurred at the transition from tight to porous volcaniclastic/volcanic units characterized by in-situ fragmentation. Notably, this spike represents the highest magnitude rejected-noise response observed across the entire well log interval and coincides with the sharpest decrease in RHOB. In contrast, coherence remained near background values at this depth, with a minimum value of 0.98 and no discernible anomaly.

The magnitude and location specificity of this noise response is significant. The fact that the strongest noise anomaly in the well occurs at a stark petrophysical transition not captured by coherence supports the interpretation that rejected noise is sensitive to structural or deformation-related heterogeneity unresolved by coherence alone. This observation provides independent support for the hypothesis that rejected noise may be detecting subsidiary faulting or deformation within the Upper Cretaceous faulted system that does not generate a coherence anomaly at seismic scale.

In the non-productive well, there was no other available well log data besides NPHI and Gamma. The largest spike in rejected noise occurred at the transition from the Ariri Formation to the Barra Velha Formation. This was to be expected given that the top and bottom boundary of the Ariri Formation are two of the largest acoustic impedance contrasts within the Bacalhau seismic dataset. The second highest noise spike comes at the interface between tight carbonates, and fractured and porous volcaniclastics/volcanics. This interface was not at all registered by coherence, as it remained at approximately 1 throughout most of this section, until it reached a minimum of 0.92 at the interface between the porous and fractured volcaniclastics and the tight volcanics/volcaniclastics. Since there was no RHOB, this interface between tight and non-tight facies was where we had the highest uncertainty of whether or not the rock was actually going through a density change, since the rock type was similar. Interpretations were based solely on whether the core data report documented fractures and/or apparent porosity throughout most of the interval.

Since rejected noise is derived from seismic amplitude data, it is important to consider amplitude magnitudes along the well. In the productive well, the initial interface corresponding to the second-highest noise magnitude, marking the transition from tight to fractured or porous carbonates, is not associated with a distinct amplitude anomaly. The transition from carbonates to volcaniclastics, which coincides with the third-highest noise magnitude, corresponds to a low-magnitude amplitude anomaly that may be classified as a dim spot. The highest noise magnitude, occurring at the boundary between tight and porous/fragmented volcaniclastics, corresponds to a high-amplitude trough. These observations indicate that the relationship between rejected noise and seismic amplitude is not strictly one-to-one and varies which could depend on the nature of the petrophysical contrasts along the well.

In the non-productive well, amplitude magnitudes vary significantly and exhibit a more sinusoidal character, making it difficult to interpret in a meaningful way. This may reflect increased complexity in the seismic response due to closer proximity to the salt–carbonate interface. For both the wells, high noise magnitudes could sometimes be justified by amplitude anomalies but not in a consistent manner. At facies interfaces, rejected noise anomalies tend to increase with fracturing and porosity and decreases as they decline. The original seismic amplitudes are not as consistent in this manner. This suggests that rejected noise is capturing a more systematic response to petrophysical variability, that acoustic impedance contrasts can't always resolve on their own. A potential extension of this work could involve evaluating how fault zone envelopes estimated from rejected noise compare to the average amplitude of the reflectors within which they are measured.

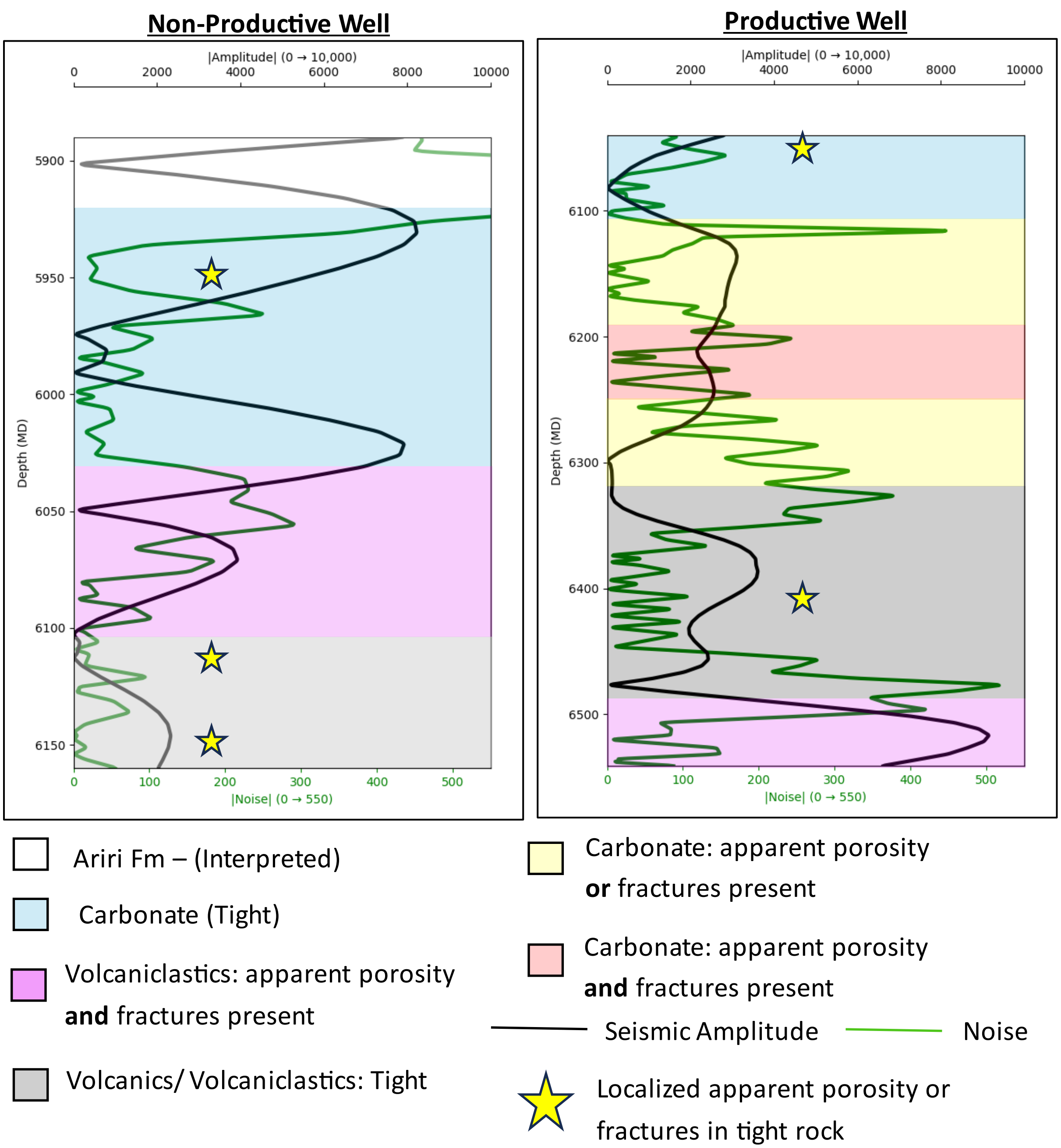

Figure 20. Noise and seismic amplitude extractions along both wells. Curves for both the rejected noise and the amplitude data are co-rendered with their respective color-coded facies (legend at the bottom of the figure). Noise increases in magnitude with increasing fractures and/or porosity at each interface (less so at the fractured and porous carbonate interval. This is likely because it is aligned with an anomalous coherence low as previously described). Seismic amplitudes do not exhibit the same pattern. Bright and dim spots are often present at interfaces but increases or decreases in magnitude do not correspond respectively to increases or decreases in apparent porosity and fractures as reliably as the rejected noise.

How Sensitive noise is to Rock Property Changes

Noise spikes corresponding to facies changes in both the productive and non-productive wells occurred within approximately 10 meters of the respective interfaces. At these depths, our vertical seismic resolution was roughly 50 meters, indicating that rejected noise consistently responded to rock property changes well below seismic resolution. In the shallower post-salt interval where fault damage zones were measured, the vertical resolution was approximately 10 meters. To clarify what is meant by damage zone extent in this seismic dataset, it is important to distinguish our definition from that used in field studies, where even microfractures may be used to separate protolith from damage zone rocks. In regions where rejected noise modeled a substantially broader damage zone than coherence, it is plausible that this response may reflect subsidiary faults below seismic resolution with connective damage zones. However, this raises the additional question of what scale of deformation structures is being detected. Given the strong correspondence between rejected noise spikes and petrophysical transitions observed in the wells, it is possible that at best, the rejected noise is responding to zones with an increased number of deformation structures on the order of meters in length. This is our interpretation of how we could define the damage zone to its outermost extent.

Complementary Behavior of Coherence and Rejected Noise

The results of this study demonstrated that coherence and rejected noise were not competing attributes, but rather complementary tools for structural interpretation. Coherence proved to be more reliable for defining fault geometries and exhibited a scaling relationship between slip and damage zone width consistent with established field data compilations, reinforcing its utility for regional fault zone characterizations. In contrast, rejected noise revealed structural complexity not consistently captured by coherence, including small offset faults and localized anomalies that may have reflected subsidiary faulting below seismic resolution. This hypothesis was further supported by well data, where rejected noise more effectively highlighted petrophysical transitions associated with void space development and mechanical deformation, even in intervals where coherence remained in background values. Collectively, these points provided the foundation for the conclusions that follow.

CONCLUSIONS

In this study we evaluated the use of coherence and structure-oriented filter (SOF) derived rejected noise for constraining fault damage zone widths within the Bacalhau 3D seismic dataset. While coherence has long been recognized as an effective tool for fault delineation, quantitative workflows for estimating damage zone width at seismic scale remain limited. A primary objective of this work was therefore to assess whether rejected noise which is traditionally treated as a processing byproduct contains structurally meaningful signal that can complement coherence and improve interpretation of fault zone architecture.

Coherence consistently provided the most stable and repeatable estimates of damage zone width. Damage zone measurements derived from coherence reproduced the near 1:1 linear scaling relationship between fault slip and damage zone width documented in outcrop-based field studies. This agreement supports the use of coherence-derived damage zone width estimates and demonstrates that seismic-scale measurements can reflect established field relationships despite inherent resolution differences.

Rejected noise exhibited more variable behavior compared to coherence. In many intervals, it mimicked stratigraphic amplitude variations and therefore could not independently define damage zone boundaries with the same reliability as coherence. However, differences in morphology revealed that noise aligned with interpreted faults displayed distinct geometric characteristics. As a result, we introduced a novel classification scheme that distinguished structurally significant noise based on these traits. This distinction was critical, especially when evaluated next to coherence-defined anomalies related to structural discontinuities.

Several key findings demonstrated the value of treating rejected noise as an interpretive attribute. Rejected noise improved fault continuity along certain small-offset faults that did not produce coherence anomalies and showed potential damage zone connectivity where coherence did not. This suggests that rejected noise may be sensitive to subtle deformation or variations below the resolution of coherence. Additionally, rejected noise consistently captured interfaces between differing lithologic facies interpreted from the Bacalhau well and core data. In 3 sampling lines, noise estimated a damage zone more than 100 meters thicker than coherence. The fact that rejected noise responded to more petrophysical changes than coherence therefore provides some support for our hypothesis that noise may be detecting subsidiary faulting beneath seismic resolution.

Improved seismic characterization of fault damage zones has implications beyond structural mapping. Damage zones influence permeability distribution, fluid migration pathways, reservoir compartmentalization, and seal integrity, making their accurate delineation critical for subsurface risk assessment. These applications extend beyond hydrocarbon development and can be used to improve renewable energy project workflows, including carbon capture and storage and geothermal reservoirs, where proper permeability and sealing capacity characterizations govern long-term performance. By refining how damage zones are interpreted from seismic data, this study contributes to more informed subsurface decision-making across a range of energy applications.

In summary, this thesis demonstrates that SOF-derived rejected noise contains meaningful structural information that when evaluated alongside coherence and calibrated to field and well data, improves seismic-scale characterization of fault damage zones. Together, these attributes provide a more complete and physically grounded framework for interpreting fault architecture in 3D seismic data.

REFERENCES

Chopra, S., and Marfurt, K. J., 2005, Seismic attributes—A historical perspective: Geophysics, 70(5), 3SO–28SO. https://doi.org/10.1190/1.2098670

Chopra, Satinder, and Kurt J. Marfurt. "Volumetric fault image enhancement — some applications." *Interpretation*, vol. 5, no. 2, 31 May 2017. https://doi.org/10.1190/int-2016-0129.1.

Fehmers, Gijs C., and Christian F. Höcker. "Fast structural interpretation with structure-oriented filtering." *Geophysics*, vol. 68, no. 4, 1 Jan. 2003, pp. 1286–1293, https://doi.org/10.1190/1.1598121.

Liao, Zonghu, et al. "Analysis of fault damage zones using three-dimensional seismic coherence in the Anadarko Basin, Oklahoma." AAPG Bulletin, vol. 103, no. 8, Aug. 2019, pp. 1771–1785. https://doi.org/10.1306/1219181413417207.

Faulkner, D. R., et al. "Scaling of fault damage zones with displacement and the implications for Fault Growth Processes." *Journal of Geophysical Research*, vol. 116, no. B5, 28 May 2011 https://doi.org/10.1029/2010jb007788.

Shipton, Z.K., and P.A. Cowie. "Damage zone and slip-surface evolution over µm to km scales in high-porosity Navajo Sandstone, Utah." *Journal of Structural Geology*, vol. 23, no. 12, Dec. 2001, pp. 1825–1844. https://doi.org/10.1016/s0191-8141(01)00035-9.

Celestino, Maria Alcione, et al. "Fault damage zones width: Implications for the tectonic evolution of the northern border of the Araripe Basin, Brazil, Ne Brazil." *Journal of Structural Geology*, vol. 138, Sept. 2020, p. 104116. https://doi.org/10.1016/j.jsg.2020.104116.

Chopra, Satinder, and Kurt J. Marfurt. "Coherence attribute applications on seismic data in various guises." *2018 AAPG Annual Convention & Exhibition*, 2018, https://doi.org/10.1306/42273chopra2018.

Marfurt, Kurt J. "Robust estimates of 3D reflector dip and Azimuth." *Geophysics*, vol. 71, no. 4, 1 Jan. 2006, https://doi.org/10.1190/1.2213049.

Kuwahara, M., K. Hachimura, S. Eiho, and M. Kinoshita, 1976, Digital processing of biomedical images: Plenum Press, 187–203.

Luo, Yi, et al. "Edge-preserving smoothing and applications." *The Leading Edge*, vol. 21, no. 2, 1 Feb. 2002, pp. 136–158, https://doi.org/10.1190/1.1452603.

Rodrigues Maas, Marcus Vinicius, et al. "Transfer learning from seismic data for predicting reservoir productivity and lithologies for upstream optimization." *Interpretation*, vol. 14, no. 1, 1 Feb. 2026, https://doi.org/10.1190/int-2025-0010.

Moreira, J.L.P., Madeira, C.V., Gil, J.A., Machado, M.A.P. 2007. Bacia de Santos. Rio de Janeiro. Boletim de Geociências da Petrobras, v. 15, n. 2, 531-549.

Baptista, Rui Jorge, et al. "The presalt Santos Basin, a super basin of the twenty-first century." *AAPG Bulletin*, vol. 107, no. 8, Aug. 2023, pp. 1369–1389, https://doi.org/10.1306/04042322048.

Louback, Viktor Souto, et al. "Aptian flood basalts in Bacalhau Oil and gas field: Petrogenesis and geodynamics of post-rift Tholeiites in the pre-salt sequence of Santos Basin, Brazil." *Contributions to Mineralogy and Petrology*, vol. 178, no. 3, 18 Feb. 2023, https://doi.org/10.1007/s00410-023-01995-0.

Savage, Heather M., and Emily E. Brodsky. "Collateral damage: Evolution with displacement of Fracture Distribution and secondary fault strands in fault damage zones." *Journal of Geophysical Research*, vol. 116, no. B3, 31 Mar. 2011, https://doi.org/10.1029/2010jb007665.

Qi, Xuan, and Kurt Marfurt. "Volumetric aberrancy to map subtle faults and flexures." *Interpretation*, vol. 6, no. 2, 1 May 2018, https://doi.org/10.1190/int-2017-0114.1.

Xing, Yuzhong, et al. "Fracture properties and their impacts on performance in carbonate reservoir, Central Block B on the right bank of Amu Darya." *Lithosphere*, vol. 2022, no. Special 12, 23 July 2022, https://doi.org/10.2113/2022/5335113.

Ostermeijer, Giles A., et al. "Damage zone heterogeneity on seismogenic faults in crystalline rock; a field study of the Borrego Fault, Baja California." *Journal of Structural Geology*, vol. 137, Aug. 2020, p. 104016, https://doi.org/10.1016/j.jsg.2020.104016.

APPENDICES

Appendix A: Original Amplitude Volume vs. SOF Volume

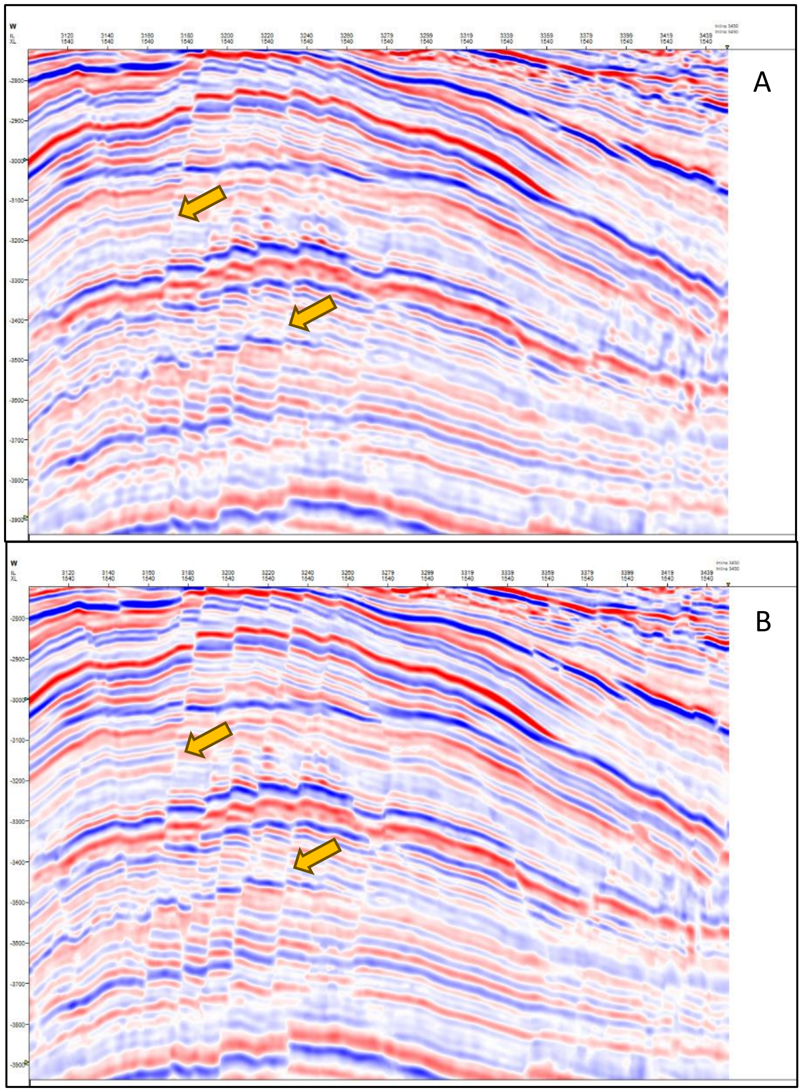

Appendix A. Figure 1. Crossline 1540 of seismic amplitude data before (**1A**) and after (**1B**) SOF. Orange arrows highlight areas with enhanced sharpness around the fault plane.

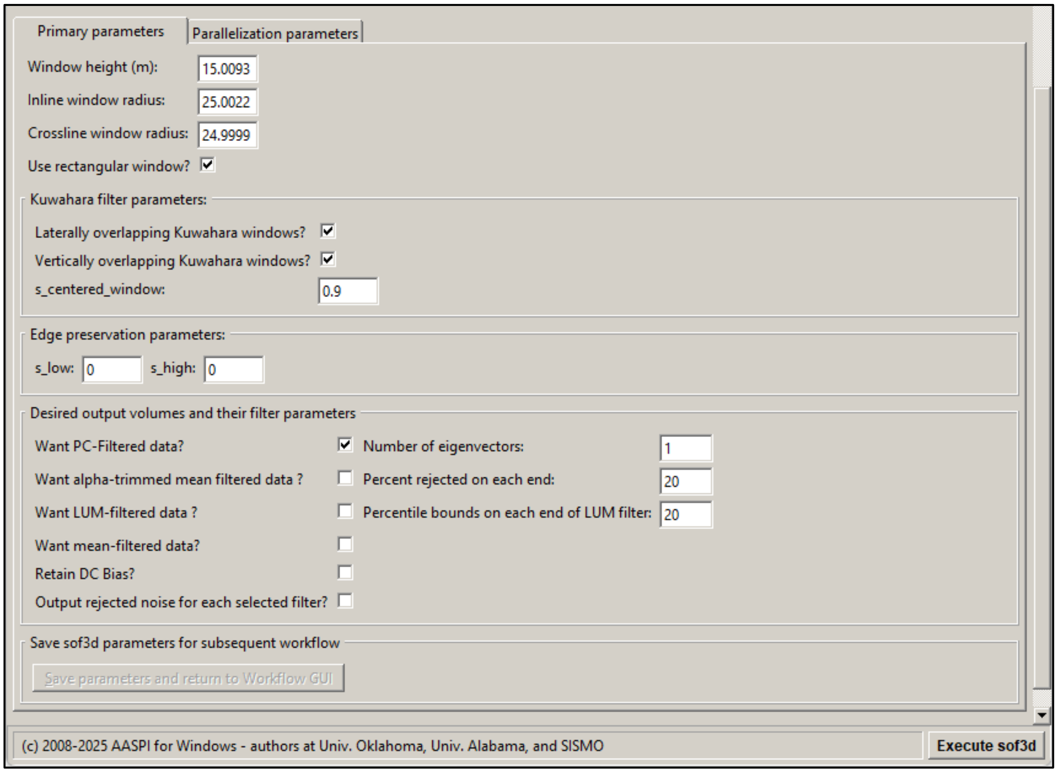

Appendix A. Figure 2. SOF user interface. S_centered, s_low and s_high are the coherence threshold values defined by the interpreter that guides how the filter operates (refer to Figure 2). The number of principal components (PC) calculated during computation can be adjusted by selecting the number of eigen vectors. We chose the 1st eigen vector to build the filtered trace from (i.e. 1st PC). The radius of the analysis window was set to default which is the bin size of the survey. This effectively would include 9 traces in the analysis window.

Appendix B: Damage Zone Widths Table & Sampling Line Example

DZ Widths Table

Slip	DZ Width (Noise)	DZ Width (Coh)
37	112	89
40	98	70
52	130	107
44	98	60
39	103	67
42	150	78
61	143	120
74	168	149
50	210	129
30	203	73
54	117	97
23	60	49
27	100	71
99	N/A	158
26	188	85
93	N/A	140
28	N/A	75
20	N/A	73
84	N/A	134
21	N/A	71
59	N/A	110
83	N/A	107
41	N/A	77
32	N/A	100
29	N/A	90
32	N/A	97
27	N/A	104
37	N/A	82
50	N/A	88
38	200	108

Extracted Values

coh10	rn10
0.89989	411.1469
0.94924	-59.2377
0.98091	-138.843
0.97453	178.5829
0.98254	459.5885
0.98585	777.4848
0.92218	1106.445
0.53031	-387.735
0.75718	1556.519
0.91544	1818.907
0.96482	1003.894
0.98017	296.544
0.99025	-55.3718
0.99373	-173.972

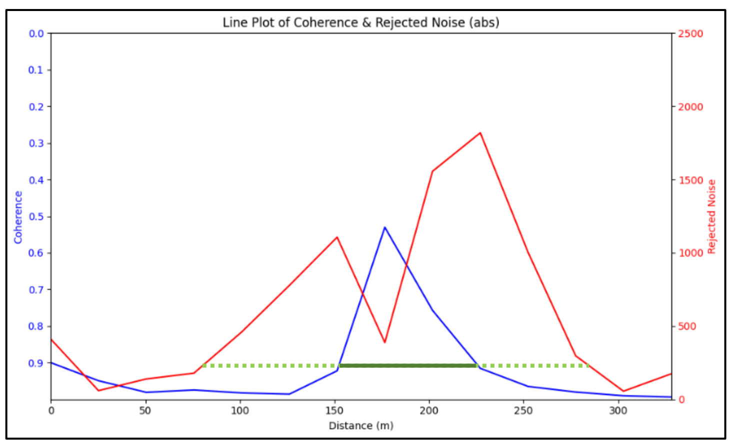

Appendix B. Figure 1. Sampling line workflow expanded. The values in the table on the far left are the recorded values that Figure 13 is plotting. The entry highlighted in red and expanded to the right are the sampling line values recorded along the sampling line in Petrel that determined those estimated damage zone widths based off the coherence and noise. N/A values are areas where stratigraphic mimicking noise was too abundant adjacent to the measured fault, so only coherence estimates were recorded. The resulting sampling line is depicted in the bottom right. The damage zone width estimated by the coherence is shown in dark green while the estimation from the noise is shown by the dotted light green line.

Appendix C: Frequency Spectrums

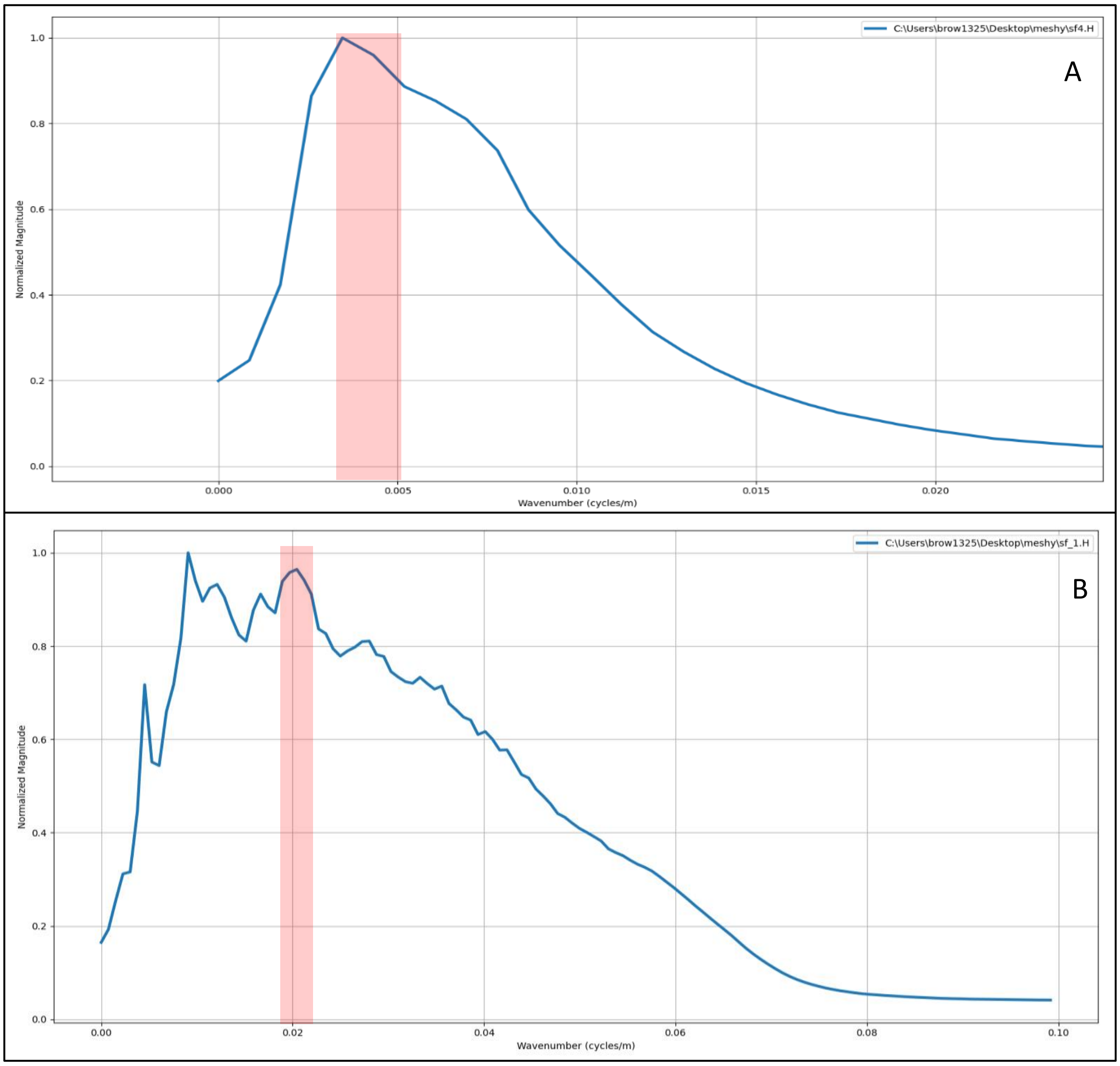

Appendix C. Figure 1. Frequency spectrums with the dominant frequency highlighted in red for our respective areas of interest. **1A)** Frequency spectrum of the seismic data that encompasses the well log intervals. Red rectangle highlights the range of the most dominant frequencies. Range is centered about 0.0047 cycles/m which translates to a vertical resolution of approximately 53 meters. **1B**) Frequency spectrum of the seismic data that encompasses the faults where we estimated damage zone widths in this study. Red rectangle again highlights the range of the dominant frequencies which is centered about approximately 0.021 cycles/m which corresponds to a vertical resolution of 12 meters.

Appendix D: Python Code Used in This Study

Part 1: Python Code for Sampling Line Creation

```
import pandas as pd
import matplotlib.pyplot as plt
import numpy as np
df = pd.read_excel("Line reader2.xlsx", usecols=["coh10", "rn10"])
df = df.dropna(subset=["coh10", "rn10"])
df['distance'] = np.linspace(0, 328, len(df))
df['rn10'] = df['rn10'].abs()
fig, ax1 = plt.subplots(figsize=(10, 6))
ax1.plot(df['distance'], df['coh10'], color='blue', label='coh6')
ax1.set_xlabel('Distance (m)')
ax1.set_ylabel('Coherence', color='blue')
ax1.set_xlim(0, 328)
ax1.set_ylim(1, 0.2)
ax1.set_yticks(np.arange(0.9, -0.1, -0.1))
ax1.tick_params(axis='y', labelcolor='blue')
ax2 = ax1.twinx()
ax2.plot(df['distance'], df['rn10'], color='red', label='rn')
ax2.set_ylabel('Rejected Noise', color='red')
ax2.set_ylim(0, 2500)
ax2.tick_params(axis='y', labelcolor='red')
plt.title("Line Plot of Coherence & Rejected Noise (abs)")
plt.tight_layout()
plt.show()
plt.title("Line Plot of 'coh' and 'rn'")
```

```
plt.tight_layout()
plt.show()
```

Part 2: Python Code for Visualizing Well Data Extractions

```
import pandas as pd
import numpy as np
import matplotlib.pyplot as plt

df = pd.read_excel("trace4_center_MD_ge6040.xlsx")
for col in ["MD", "Noise", "Amplitude", "Coh", "MDG", "Gamma", "NPHI", "RHOB"]:
    df[col] = pd.to_numeric(df[col], errors="coerce")
df["Gamma"] = df["Gamma"].clip(upper=155)
df["RHOB"]  = df["RHOB"].clip(upper=2.95)
seis_noise = df[["MD", "Noise"]].dropna().sort_values("MD").copy()
seis_amp   = df[["MD", "Amplitude"]].dropna().sort_values("MD").copy()
seis_coh   = df[["MD", "Coh"]].dropna().sort_values("MD").copy()
triple     = df[["MDG", "Gamma", "NPHI", "RHOB"]].dropna().sort_values("MDG").copy()
seis_noise["NoiseAbs"] = seis_noise["Noise"].abs()
seis_amp["AmpAbs"]     = seis_amp["Amplitude"].abs()
SEIS_WINDOW = 3
LOG_WINDOW  = 25
seis_noise["NoiseAbs_s"] = seis_noise["NoiseAbs"].rolling(
    window=SEIS_WINDOW, center=True, min_periods=1
).mean()
```

```
seis_amp["AmpAbs_s"] = seis_amp["AmpAbs"].rolling(
    window=SEIS_WINDOW, center=True, min_periods=1
).mean()
seis_coh["Coh_s"] = seis_coh["Coh"].rolling(
    window=SEIS_WINDOW, center=True, min_periods=1
).mean()
triple["Gamma_s"] = triple["Gamma"].rolling(
    window=LOG_WINDOW, center=True, min_periods=1
).mean()
triple["NPHI_s"] = triple["NPHI"].rolling(
    window=LOG_WINDOW, center=True, min_periods=1
).mean()
triple["RHOB_s"] = triple["RHOB"].rolling(
    window=LOG_WINDOW, center=True, min_periods=1
).mean()
DEPTH_TOP = 6040
DEPTH_BASE = 6541
NOISE_MIN, NOISE_MAX = 0, 550
AMP_MIN, AMP_MAX     = 0, 10_000
GAMMA_MIN, GAMMA_MAX = 0, 155
NPHI_MIN, NPHI_MAX   = -0.15, 0.45
RHOB_MIN, RHOB_MAX   = 1.95, 2.95  # reversed in plotting
COH_MIN, COH_MAX = 0.75, 1.00
def plot_seis_with_triple(seis_df, seis_col, seis_label, seis_xlim, reverse_x=False,
seis_color="red"):
    fig, ax = plt.subplots(figsize=(6, 9))
```

```
ax.plot(seis_df[seis_col], seis_df["MD"], color=seis_color, linewidth=1)
ax.set_ylim(DEPTH_TOP, DEPTH_BASE)
ax.invert_yaxis()
if reverse_x:
    ax.set_xlim(seis_xlim[1], seis_xlim[0])
else:
    ax.set_xlim(seis_xlim[0], seis_xlim[1])
ax.set_ylabel("Depth (MD / MDG)")
ax.set_xlabel(seis_label, color=seis_color)
ax.tick_params(axis="x", colors=seis_color)
ax.spines["top"].set_visible(False)
ax_g = ax.twiny()
ax_g.plot(triple["Gamma_s"], triple["MDG"], color="green", linewidth=1)
ax_g.set_ylim(DEPTH_TOP, DEPTH_BASE)
ax_g.invert_yaxis()
ax_g.set_xlim(GAMMA_MIN, GAMMA_MAX)
ax_g.set_xlabel("Gamma (0 → 155)", color="green")
ax_g.tick_params(axis="x", colors="green")
ax_g.spines["bottom"].set_visible(False)
ax_n = ax.twiny()
ax_n.plot(triple["NPHI_s"], triple["MDG"], color="blue", linewidth=1)
ax_n.set_ylim(DEPTH_TOP, DEPTH_BASE)
ax_n.invert_yaxis()
ax_n.set_xlim(NPHI_MIN, NPHI_MAX)
ax_n.set_xlabel("NPHI (-0.15 → 0.45)", color="blue")
ax_n.tick_params(axis="x", colors="blue")
```

```
    ax_n.spines["top"].set_position(("axes", 1.08))
    ax_n.spines["bottom"].set_visible(False)
    ax_n.spines["left"].set_visible(False)
    ax_n.spines["right"].set_visible(False)
    ax_r = ax.twiny()
    ax_r.plot(triple["RHOB_s"], triple["MDG"], color="black", linewidth=1)
    ax_r.set_ylim(DEPTH_TOP, DEPTH_BASE)
    ax_r.invert_yaxis()
    ax_r.set_xlim(RHOB_MAX, RHOB_MIN)
    ax_r.set_xlabel("RHOB (2.95 → 1.95)", color="black")
    ax_r.tick_params(axis="x", colors="black")
    ax_r.spines["top"].set_position(("axes", 1.16))
    ax_r.spines["bottom"].set_visible(False)
    ax_r.spines["left"].set_visible(False)
    ax_r.spines["right"].set_visible(False)
    plt.tight_layout()
    plt.show()
plot_seis_with_triple(
    seis_df=seis_noise,
    seis_col="NoiseAbs_s",
    seis_label="|Noise| (0 → 550)",
    seis_xlim=(NOISE_MIN, NOISE_MAX),
    reverse_x=False,
    seis_color="red"
)
plot_seis_with_triple(
```

```
    seis_df=seis_amp,
    seis_col="AmpAbs_s",
    seis_label="|Amplitude| (0 → 10,000)",
    seis_xlim=(AMP_MIN, AMP_MAX),
    reverse_x=False,
    seis_color="red"
)
plot_seis_with_triple(
    seis_df=seis_coh,
    seis_col="Coh_s",
    seis_label="Coh (1.00 → 0.75)",
    seis_xlim=(COH_MIN, COH_MAX),
    reverse_x=True,
    seis_color="red"
)
```